Óbuda University

Doctoral Dissertation

Development of novel measurement methods for neuroscientific research and dentistry

Gábor Orbán

Supervisor:
Gergely Márton, PhD

Doctoral School on Materials Sciences and Technologies

Budapest, March 24, 2021

Komplex vizsga bizottság:

Elnök:	Horváth Zsolt József, DSc, egyetemi tanár, ÓE
Tagok:	Csikósné Pap Andrea, PhD, egyetemi docens, ÓE
	Harsányi Gábor, DSc, egyetemi tanár, BME

Nyilvános védés bizottsága:

Opponensek:	Csikósné Pap Andrea, PhD, egyetemi docens, ÓE
	Somogyvári Zoltán, PhD, ELKH Wigner FK RMI
Elnök:	Horváth Zsolt József, DSc, professor emeritus, ÓE
Titkár:	Kovács Tünde Anna, PhD, egyetemi docens, ÓE
Tagok:	Nemcsics Ákos, DSc, egyetemi tanár, ÓE
	Baji Zsófia, PhD, tudományos munkatárs, ELKH EK MFA
	Bognár György, PhD, egyetemi docens, BME VIK EET

Nyilvános védés időpontja:
2021. 05. 04.

Nyilatkozat a munka önállóságáról, irodalmi források megfelelő módon történt idézéséről

Alulírott *Orbán Gábor* kijelentem, hogy a *Development of novel measurement methods for neuroscientific research and dentistry* című benyújtott doktori értekezést magam készítettem, és abban csak az irodalmi hivatkozások listáján megadott forrásokat használtam fel. Minden olyan részt, amelyet szó szerint, vagy azonos tartalomban, de átfogalmazva más forrásból átvettem, a forrás megadásával egyértelműen megjelöltem.

Budapest, March 24, 2021

Orbán Gábor

Nyilatkozat a nyilvánosságra hozatalról

Alulírott *Orbán Gábor* hozzájárulok a *Development of novel measurement methods for neuroscientific research and dentistry* című doktori értekezésem interneten történő nyilvánosságra hozatalához az alábbi formában:

- **korlátozás nélkül**;
- elérhetőség csak magyarországi címről;
- elérhetőség a fokozat odaítélését követően 2 év múlva, korlátozás nélkül;
- elérhetőség a fokozat odaítélését követően 2 év múlva, csak magyarországi címről.

Budapest, March 24, 2021

Orbán Gábor

Contents

List of acronyms

Acronym	Reconstitution
aCSF	Artificial cerebrospinal fluid
AP	Anteroposterior
BCI	Brain-computer interface
CCD	Charge-coupled device
CW	Cranial window
ECoG	Electrocorticography
EEG	Electroencephalography
FFT	Fast Fourier transform
GEVI	Genetically encoded voltage indicators
HAS	Hungarian Academy of Sciences
IIR	Infinite impulse response
IR	Infra red
ITO	Indium tin oxide
LFP	Local field potential
MEA	Microelectrode array
MEMS	Micro-electromechanical system
ML	Mediolateral
PCA	Principal component analysis
QD	Quantum dot
RCNS	Research Centre for Natural Sciences
SEM	Scanning electron microscope
SUA	Single unit activity
UV	Ultra violet

Chapter 1

Introduction

Electrophysiology is the scientific area of observation and study of the electrical properties of the biological cells and tissues. This dissertation could be split into two parts according to this definition. Both main research projects which will be presented herein are based on electrophysiology. The aim of the first one is the simultaneous utilization of an electrophysiological measurement method and an optical imaging process for neuroscientific research, where the principal targets of observation are neurons. The second presented research topic is related to human dental structures. During this research an electrical property of a biological tissue, namely the electrical impedance of the human dentin has been measured, and a formula has been determined to evaluate its dependency on geometric thickness and signal frequency.

During my scientific activities I have studied and observed the central nervous system and I have taken part in neural electrode system development and validation projects from the conceptualization to the performance of *in vitro* and *in vivo* experiments. These research topics led me to the results of my first thesis group, thus in the first part of the introduction chapter the electrophysiological methods will be reviewed which are used in the field of neuroscience.

One of my aims was to observe the peripheral nervous system in the pulp of the human teeth, by using a measurement method on dentin. In order to reach this goal, it was essential to perform numerous electrophysiological experiments on human teeth to observe their electrical properties. Since my second thesis point is based on the results of this observation, therefore in the second part of the introduction chapter I give an overview of the experimental and clinical utilization of electrophysiological methods in the field of dentistry.

The scientific work related to the simultaneous electrophysiology and two-photon

imaging was performed at the Comparative Psychophysiology research group under the leadership of Prof. Dr. István Ulbert at the Institute of Cognitive Neuroscience and Psychology, Research Centre for Natural Sciences, Eötvös Loránd Research Network. The scientific activity in the field of dentistry was executed at the Department of Oral Diagnostics, Faculty of Dentistry, Semmelweis University with the contribution and guidance of Prof. Dr. Csaba Dobó Nagy.

The specific aims of the dissertation will be defined after the first chapter, which is followed by the description of the various factors which led me to reach these scientific aims.

1.1 Electrophysiology - a short overview

By electrophysiology we mean the observation of electrical functions of the nervous system. The measurement principles of electrophysiology rely on the forms of information transfer among neurons, which form the basis of our nervous system. During this transfer transmembrane currents rise and fall [1]. Neurons can process signals and communicate with each other partly via these transmembrane currents. Since the electrical conductance of the extracellular space is finite [2], the membrane currents create electric potential differences inside the neural tissue [3], which propagate outside the neural tissue as well, e.g. onto the scalp [4]. The measurement of these electric potential differences makes the observation of the functions of specific brain regions as well as the connection between brain regions possible [5, 6]. Electrophysiological measurements helped neuroscientists diagnose and to observe the causes of some neurological disease such as autism or epilepsy [7,8], and led to the development of treatments which make neural diseases like Parkinson's disease asymptomatic [9]. Electrophysiological measurement methods which yield signals of neural activities with high information content, such as electroencephalography (EEG), electrocorticography (ECoG) and intracortically implanted high density microelectrode arrays (MEAs), have vastly contributed to the progress of neuroscience and brain-computer interfacing (BCI) [10–13]. In the next subsections these measurement methods will be reviewed.

1.1.1 Electroencephalography

Electroencephalography is a noninvasive electrophysiological measurement method suitable for recording electrical activity of neuron populations within the cerebrum. EEG electrodes are placed on the scalp to measure potential differences resulting

from membrane current of the neurons [14]. It became a widespread neuroimaging method since it is relatively cheap, noninvasive, and it can record the potential changes of the neural tissue with a temporal resolution in the range of milliseconds [15]. Since the measurable electrical activity of the neurons on the scalp is usually a summed and synchronized signal, the main disadvantage of the utilization of EEG is its low spatial resolution [14] and the fact that EEG source localization is an inverse problem, as potential differences on the surface of a spheroidal object can be generated in infinite number of variations of internal source patterns. This prevents perfect spatial localization of the neural activities from the signals recorded on the scalp [16]. Furthermore, the signal-to-noise ratio of EEG is poor due to the insulating effect of the skull. In spite of these disadvantages, EEG is a ubiquitous measurement method in neuroscientific experiments [17],and in the clinic for diagnostic [8, 18] and therapeutic [19] purposes. EEG has a huge impact on brain-computer interface development as well [20, 21].

1.1.2 Electrocorticography

Electrocorticography is similar to EEG but the electrodes are placed on the surface of the brain so as to record the electrical activity of the neural tissue [22]. This measurement method has benefits comparing to EEG since the electrodes on the surface of the brain eliminate the insulating effect of the skull, thus it has better signal-to-noise ratio and spatial resolution [23]. The main disadvantage of ECoG is its invasiveness so it is used only under particular consideration in human cases. In terms of animal experiments, ECoG was an important method for creating brain function mapping and observing the connectivity of specific areas of the brain [24]. One of the most widespread clinical utilization of ECoG is the localization of the epileptic foci in order to minimize the volume and the functional effect of the necessary lesion during surgery [25]. Similarly to EEG, ECoG is a promising method in the development of BCIs for controlling limb prostheses [13, 26] and expanding communication abilities [27].

1.1.3 Implanted microelectrode arrays

The application of implanted microelectrode arrays is a highly invasive measurement method, on the other hand these devices are not only capable of recording the summed bioelectrical activities of neuron populations (i.e. local field potentials, LFPs), but they can also detect individual activities of neurons (i.e. single unit activities, SUAs) [28, 29]. These methods had an instrumental role in the functional

mapping of the brain [30] and they are still the ultimate solution when high spatial and temporal resolution are required [13, 31, 32]. In the last few years significant improvement was reached in the field of thought controlled communication due to the utilization of intra-cortical MEAs. Such communication is essential for people with locked-in syndrome, which is the inability to move and to speak despite being fully awake, due to for example a brainstem injury. Monitoring the signals of specific brain region can allow the control of a cursor on a computer screen or typing on a virtual keyboard [33–36]. These kind of BCIs are the key for movement restoration too. If neural interface controlled assistive devices could be driven accurately and with low latency that would be helpful to people with paralysis or limb loss too. Previous studies on monkeys show that BCIs are able to restore broken neural connections between the brain and a limb (or a prosthetic limb) via the utilization of inctracortical electrodes [37–40]. Recent researches present promising results in the application of these kind of BCIs in human patients with paralysis [11, 41–43]. Most BCIs which were created to help people with limb paralysis or brainstem injury are based on a specific intracortical MEA, the UTAH array (Blackrock Microsystems, Salt Lake City, USA), which is a silicon based MEA with 96 electrodes on shanks in a matrix arrangement designed to record the electrical potentials in a volume of a specific region of the cerebral cortex, as it is shown in Figure 1.1.

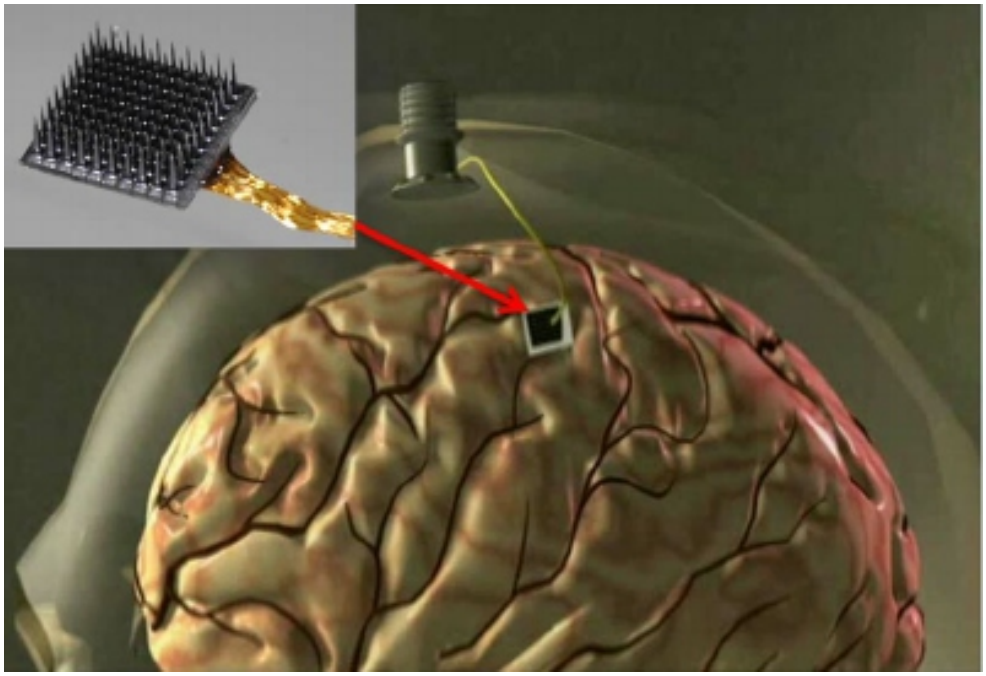

Figure 1.1: *An implanted UTAH array can form the basis of BCI devices for subjects whose normal neural information pathways are not functioning due to physical damage or disease [44]*

However, the spatial range of the SUA detection capability of the implanted sensors is limited to the immediate surroundings of the electrode sites, i.e. hundred micron

wide volumes [45]. Furthermore, the long term use of implanted MEAs is corrupted by the degradation of their performance over weeks or months, let alone years [46–48]. The underlying causes range from material failures [49, 50] to the deteriorative effects of the immune response to the implants [51–53].

1.2 Combining electrophysiology with optical imaging

In the last few decades, various optical imaging methods became widely used in neuroscience, which can render wide brain regions observable with high spatial resolution [54–58]. Furthermore, the application of two-photon microscopy with fluorescent calcium indicators makes the monitoring of neural activity (e.g. action potentials of individual cells) possible [59–62].

The two-photon laser scanning microscopy is a long-established procedure in the field of neuroscience [63], which is based on the physical effect of the two-photon excitation. During the two-photon imaging the fluorophore molecule is activated with two lower energy photons then it decays back to its fundamental state while it has a photon emission with lower energy than the sum of the two exciting photons. The application of two exciting photons allows us to define the volume of the neural tissue where we would like to observe the fluorescence activity but high photon concentration within the observed volume is required which can be reach by the utilization of high power femtosecond pulse synchronized laser [64]. The focal length of fluorescence microscope objectives can exceed 12 mm [65], which allows the implantation of depth MEAs into the optical cranial window (CW) [66]. However, the high density MEAs can cover the observation area under the array of the electrode field. To resolve this problem, MEAs based on transparent substrates and transparent conductive layers have been developed as it is representatively shown in Figure 1.2.

The most commonly used transparent substrates are the polyimide and the SU-8. Polyimide is used as an insulator and passivation layer in the manufacturing process of integrated circuits and micro-electromechanical systems (MEMS) chips for protecting the electronic components from moisture and mechanical effects, while in neuroscience it is often used as a flexible insulator substrate for MEAs [68, 69]. Preparation of a polyimide substrate is relatively easy as it can be patterned with dry etching or with photolithography by ultra violet light (UV) [**?**] after heat treatment. Polyimide has an optical transmittance of more than 85% in the visible light region [70] which makes it suitable for a substrate material of implanted MEAs. SU-8 is an epoxy-based negative-tone photoresist which can patterned with near

UV lithography. It is commonly used for fabricating MEMS and microfluidic systems since it is suitable for high aspect ratio applications [71]. Its dense crosslinked structure offers mechanical stability, yet it has high transparency over 360 nm. Over the wavelength of 500 nm the transmittance of SU-8 exceeds 95% [72].

The fabrication of transparent MEAs requires the conductive layer to be prepared from transparent materials too. In this regard, graphene is a promising material. Polymer based graphene MEAs are flexible, biocompatible and transparent on a wide wavelength ranging from UV to infrared (IR) so they are suitable for electrophysiological measurements and optical observations too [67]. Graphene layers can be produced with chemical vapor deposition. Another suitable transparent conductive layer material for electrophysiological measurements is the indium tin oxide (ITO) [73]. The preparation of ITO is easier than the preparation of graphene, although ITO has the optical transmittance of only 80% in the relevant wavelengths which is less than the 90% transmittance of graphene. ITO layer production can be performed with chemical vapor deposition as well.

There are conductive polymers which could form the electrodes of the MEA as well. Conducting polymers have attracted much interest as suitable matrices of biomolecules and have been used to enhance the stability, speed and sensitivity of various biomedical devices. They are easy to synthesize and versatile because their properties can be readily modulated by surface functionalization techniques [74, 75]. On the surface of the electrode sites of neural implants conductive polymers are

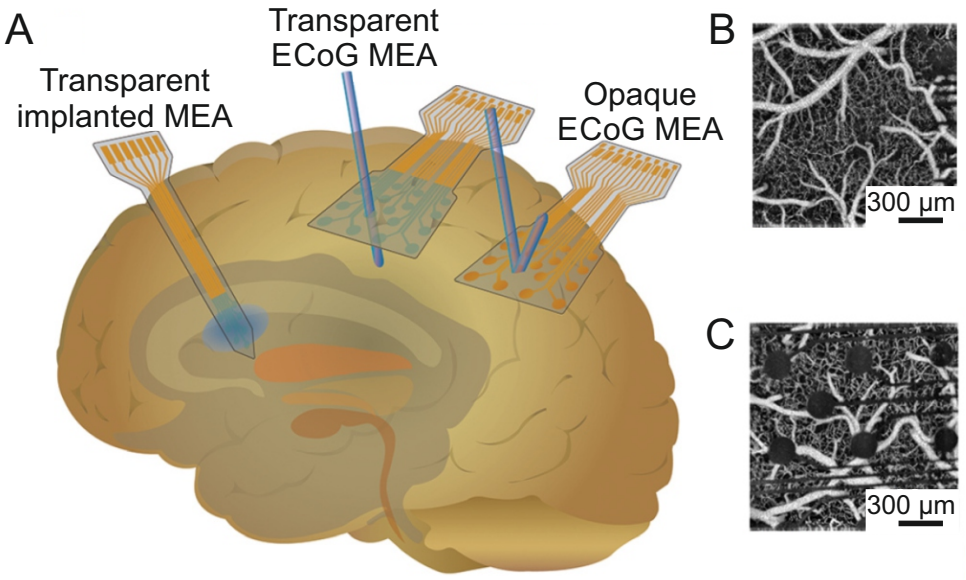

Figure 1.2: *Advantages of transparent MEAs (A). Comparison of transparent substrate based MEAs with transparent graphene electrodes (B) and opaque platinum electrode (C) on optical coherence tomography images [67]*

used for increasing long term cell stability and higher signal to noise ratio by decreasing the electrode impedances [76]. The commonly used conductive polymers on neural interfaces are the polypyrrole/peptide [77], PEDOT (i.e. Poly(3,4-ethylenedioxythiophene)) [78,79], polythiophene [80]. With the utilization of conductive polymers neuroscientists can achieve better electrode-neural tissue connection and decreased immune response near the electrodes [78]. Conductive polymers could be used as electrodes similarly to graphene or ITO, but it seems to be too difficult to synthesize a conductive and transparent polymer layer, moreover the preparation of polymer structure with wide range of optical transmittance is quasi impossible [81].

Although the proper transparent layer from conductive polymers has yet to be developed, they can be applied for another purpose when we aim for combining the implanted MEAs with the optical imaging. This application is based on quantum dot (QD) preparation from them. MEA electrodes covered by fluorescent QDs can indicate the location of the conductive site during two-photon imaging, thus it helps to perform optical imaging and electrophysiological recording from the same tissue region. Fluorescent QDs can be prepared from PEDOT by deposition of molecules on the surface of a conductive polymer (ITO) [82, 83]. The deposited PEDOT layer can be removed by ultrasound and it goes through several filtering steps, before it is deposited on the surface of a neural electrode [83]. Thus prepared molecules are already fluorescent so they can be used in fluorescence optical imaging as markers as shown in Figure 1.3.

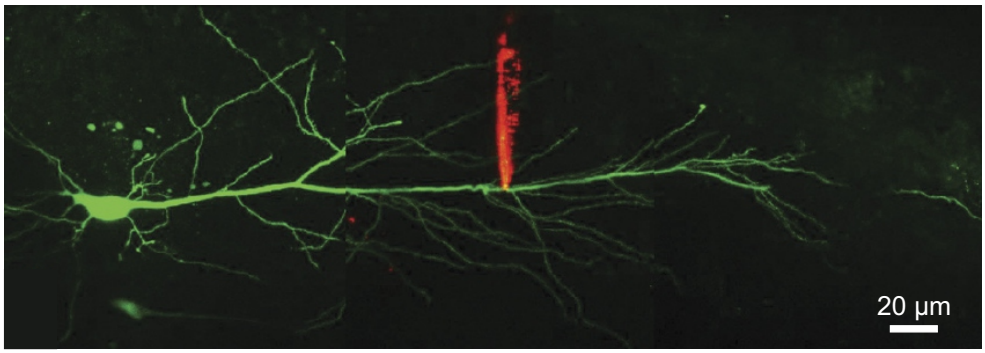

Figure 1.3: *Two-photon imaging of patch-clamp pipette filled with a solution containing fluorescent QDs, inserted into the neural tissue. The tissue had been injected with fluorescent markers [82]*

1.2.1 Simultaneous electrophysiological and optical measurement method in the field of neuroscience

Simultaneous application of depth MEAs for extracellular electrophysiology and two-photon imaging could allow neuroscientists to observe activities of individual

neurons with good spatial and temporal resolution at the same time, thus the more precise and complex pieces of information could be obtained from neural activity [84]. The extension of high density intracortical recordings with simultaneous two-photon microscopy would enable three dimensional optical monitoring of the structural features of the cells located close to the electrode. Nonetheless, the co-localized and simultaneous application of two-photon imaging and electrophysiological measurement by MEAs remains challenging, partly because of the photoelectric artefacts on the electrophysiological recordings caused by the imaging laser [85]. The artefacts generally appear as huge sawtooth-like waves. The main frequency of such waves correspond to the imaging frame rate of the applied two-photon laser. The frame rate of the imaging is indeterminate, moreover, the sharp shape of the waves and other effects introduce various harmonics other than the main frequency, thus elimination of the photoelectric artefacts requires more subtle methods than applying e.g. a notch filter. Comb filters have already been successfully used for decreasing stimulus artefacts [86] and 50 Hz low frequency noise [87] from electrophysiological signals, while adaptive filters are utilized e.g. in brain-computer interface development [88,89], in simultaneous measurements of real-time magnetic resonance imaging and electrocardiogram recordings [90], in fetal electrocardiogram analysis [91], etc.

1.3 Electrophysiology in the field of dentistry

Hard tissues, like the human bone or dentin, can be characterized with electrical properties such as intrinsic resistivity, electrical conductivity, dielectric constant or capacitance. I have performed observations on human dentin thus before the overview of the experimental and clinical utilization of electrophysiological methods in the field of dentistry a short introduction will be given about the underlying principles of these methods.

Dentin is one of the major hard tissue components of teeth. It can be found under the enamel and it surrounds the entire pulp. This tissue contains micro channels projecting radially from the pulp to the enamel called dentin tubules. The density of dentin tubules near the pulp on the inner dentin is $55000 - 75000/mm^2$, near the enamel on the outer dentin it is $15000 - 20000/mm^2$. The diameter of the tubules is different as well, near the pulp they are approximately $3 - 4$ μm wide, on the border of the dentin-enamel their width is approximately 1 μm [92–96]. A representative scanning electron microscope (SEM) (Carl Zeiss AG,Oberkochen, Germany) image of the dentin tubules is shown in Figure 1.4. The surface of the dentin near the pulp is covered with odontoblast cells which have the biological function of the

dentinogenesis, the formation of dentin [97]. Axons of odontoblasts, collagen fibers and the axons of dental nerves can be located in the dental tubules which makes the inner dentin more sensitive during dental treatment. The dentin tubules are filled with ionized dentinal fluid thus if the dentin becomes exposed the bioelectrical activity of the nerves placed in the pulp becomes measurable on the surface of the dentin. This method is called dentin recording.

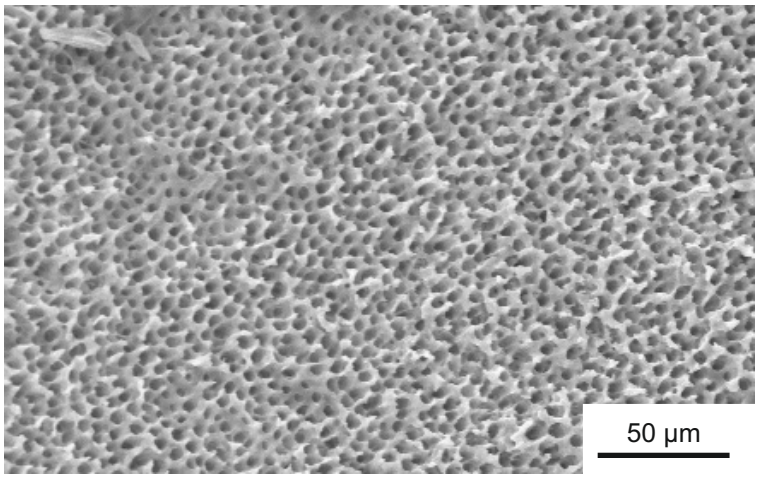

Figure 1.4: *Scanning electron microscope (SEM) image of dentin tubules of an examined dentin disk*

1.3.1 The dentin recording

Dentin tubules are able to convey both the harmful and medical substances. Bacteria produced toxins may reach the pulp through the tubules which can irritate the nerves in the pulp thus they evoke dental pain [98]. The dental pain, which can be felt during a dental treatment because of mechanical, thermal or hydrostatic stimuli, is conveyed through the dental tubules too. Dentin recording is based on the observation method of the dental fluid flow and the ion current through the dentin tubules.

Dentin recording can allow us to observe the process of dental pain and pulp inflammation which may led us to localise the source of the stimulus which caused the sensation [99]. These techniques also let the fluid flow through the tubules to be inspected and facilitate the examination of the neural control of the fluid flow [100–103]. In order to record one dental nerve activity separated from the others it is necessary to develop electrodes with small size [104]. The changes of the hydrostatic pressure of the dental fluid in the dental tubules have also been measured to calculate the electrical field of the pulp [105]. Beyond these observations

several experiments aimed to track the effect of some kind of stimulus via measuring the bioelectrical activity of tooth nerves [106]. Thus performed pulp sensibility testing has been and still remains a very helpful aid in endodontic diagnosis [107]. The application of these measurements to determine the underlying cause of dental pain have also been a subject of research [108–110]. If the pain is generated by an artificial stimulus like hydrostatic pressure on the surface of the dentin, the sensitivity of a specific dentin region can be investigated via dentin recording [111]. The response can be recorded with an *in vivo* dentin recording method at different levels of hydrostatic pressure stimuli as it is shown in Figure 1.5.

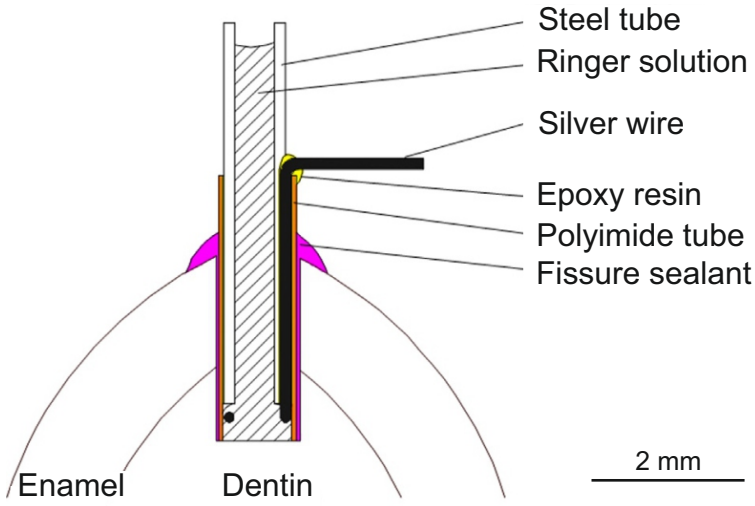

Figure 1.5: *Measurement arrangement of an* in vivo *dentin recording experiment. Hydrostatic pressure was applied* in vivo *on the surface on the dentin and the nervous response was recorded [111]*

A series of experiments have been performed utilizing different stimuli to specify the required threshold voltage and current for electrical stimulation [112]. In spite of the *in vivo* methods, these values can be defined more precisely with *in vitro* experiments. *In vitro* experiments of dentin recording are useful e.g. for the validation of resin-dentin bonding surfaces. For this purpose electrochemical impedance spectroscopy was applied as a potentially nondestructive quantitative method for measuring the stability of resin films and resin-bonded dentin over time [113]. The measurement arrangement which was used for these experiments is shown in Figure 1.6. The idea of this split chamber has formed the base of my *in vitro* measurement arrangements for my dental experiments. The only fluidic connection between the half cells of the U shaped chamber was through the dentin disk, hence the electrical circuit of the ion current was guided through the disk.

The required mechanical properties of the dentin are already well defined [114] but the electrical properties have yet to be thoroughly characterized. For this purpose,

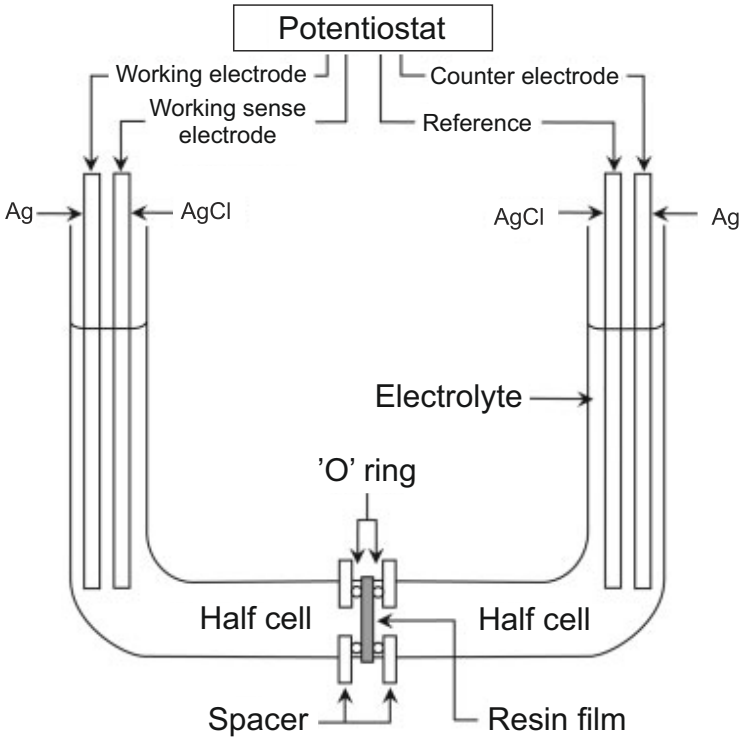

Figure 1.6: *Measuring arrangement of an* in vitro *dentin recording experiment. Split chamber was arranged in order to perform electrochemical impedance spectroscopy on dentin-resin bonding surfaces [113]*

in vitro dentin recording experiments are required. The precise determination of the electrical impedance of the dentin makes the definition of an accurate threshold voltage and current for electrical stimulation possible, but there are some difficulties [115]. The temperature of the tooth not only influences the functional properties of the tooth pulp neurons [116] but also affects the impedance of the dentin [117]. This electrical parameter also depends on the concentration of the used electrolyte (saline solution of sodium chloride) [118,119] and on the age of the tooth as well [120]. The applied measuring signal has to be AC because in case of a DC signal, polarization artefacts arise on the electrode-tooth contact area [121–123]. The exact determination of dentin impedance can reveal other parameters and can be a basis of various diagnostic methods [124]. For example, dental caries are caused by the demineralization of the dentin. This process changes both the tubules diameters and the dentin impedance [125]. Most experimental caries diagnostics methods are based on impedance measurement [125–127]. These methods have proven to be more successful than former techniques [128–131]. Measuring the impedance between an inserted electrode in a root canal of a human tooth and an outer electrode placed on the oral mucosa makes the calculation of the root canal length possible [132, 133]. Furthermore, impedance measurements can be used for defining the dentin permeability or forming the basis of the investigation of an alternative bioimpedance spectroscopy

method for the assessment of tooth structures [134]. In the last few years new methods have been developed and applied in oral sciences such as two-photon and multi-photon microscopy which were used successfully in caries diagnostics [135, 136], and γ-radiation, which can change the mechanical and electrical properties of the dentin and the enamel [137]. Impedance measurement has a prominent relevance in the definition of the electrical properties of the dentin and it can be the basis of further oral diagnostic methods that might be used in clinical practice.

Chapter 2

Specific aims

2.1 Simultaneous electrophysiological recording and two-photon imaging *in vitro*

Simultaneous utilization of implanted MEAs for extracellular electrophysiology and two-photon microscopy for optical imaging could allow the observation of activities of individual neurons with good spatial and temporal resolution, but the imaging laser generates artefacts in the electrophysiological recordings. Special noise filtering algorithm development is required to analyse the data which were recorded in the field of view of the two-photon microscope. Our aim was to perform *in vitro* experiments on mouse neocortical slices expressing the GCaMP6 genetically encoded calcium indicator for monitoring the neural activity with two-photon microscopy around the implanted MEAs. An objective of mine was to develop a complex custom-set comb filter based algorithm which could be used for noise filtering to eliminate the artefacts caused by the imaging laser. Besides the two-photon observation of the morphology near the implanted MEA, the scope of our research was to prove that this special filtering algorithm allows the detection and the sorting of SUAs from a simultaneous two-photon imaging and extracellular electrophysiological measurement.

2.2 Simultaneous electrophysiological recording and two-photon imaging *in vivo*

Having realized the special filtering algorithm for SUA detection from simultaneous two-photon imaging and extracellular electrophysiological recordings *in vitro*, our aim was to extend our investigation onto *in vivo* experiments. To reach this goal, the scope of ours was to apply a MEMS technology based MEA which would

be designed and developed in order to perform simultaneous electrophysiological recording and two-photon imaging from the same tissue region of mice brains expressing GCaMP6 genetically encoded calcium indicator. Our aim was to implant the MEA within the field of view of the two-photon imaging and perform simultaneous recordings. The previously developed algorithm was planned to improved and utilized on the recorded extracellular data to detect SUAs. The objective was to prove that combining the self-developed MEMS technology based MEA with my filtering and analyzing algorithm was capable of performing electrophysiological recording and two-photon imaging from the same tissue region at the same time.

2.3 Determination of the thickness dependent electrical impedance spectrum of the human dentin

Utilization of impedance measurement methods in dental researches makes the determination of electrical properties of human tooth possible. Although impedance measurement forms the basis of numerous oral diagnostic methods, only a limited number of studies are available focusing on the impedance of human dentin. The main goal of our experiments was to determine the thickness dependency of the impedance of the human dentin. Our model allowed the determination of a coefficient which describes the correlation between the thickness and the electrical impedance of the human dentin.

Chapter 3

Materials and Methods

3.1 Materials and methods related to the simultaneous electrophysiological recording and two-photon imaging

3.1.1 Preparation of physiological experiments

In vitro and *in vivo* experiments were performed on neural tissue of mice expressing the GCaMP6 genetically encoded calcium indicator for the monitoring of neural activity around the MEA [138, 139]. A total of five GCaMP6 mice had been anesthetized with a ketamine-xylazine solution and prepared for operation. Initial anesthesia was performed via intraperitoneal injection of a mixture of 37.5 mg/ml ketamine and 5 mg/ml xylazine at 0.1 $ml/100\ g$ body weight injection volume, body temperature was maintained at 37 °C throughout the experiments. If it was necessary, 0.05 ml of the same mixture was dosed repeatedly during the experiments. Animals for acute tests were kept and handled in accordance with the European Council Directive of 24 November 1986 (86/609/EEC), the Hungarian Animal Act, 1998 and the Animal Care Regulations of the Research Centre for Natural Sciences of the Hungarian Academy of Sciences (RCNS-HAS). The study was approved by the Institutional Animal Care and Use Committee of the Research Centre for Natural Sciences of the Hungarian Academy of Sciences (members: Dr. István Ulbert, Dr. József Topál and Péter Kottra) and the National Food Chain Safety Office of Hungary (PEI/001/695-9/2015). Animals had unlimited access to food and water, when they were awake. Each mouse was kept in a 39 cm long, 22 cm wide, 18 cm high cage. They were under deep anesthesia during surgery (and during the recording sessions in case of *in vivo* measurements) as well as at the time of sacrifice. During anesthesia, paraffin oil was administered to their eyes to prevent them from drying. Efforts were made to minimize animal suffering and to reduce the number of animals

used. They were sacrificed by the injection of a lethal dose of ketamine/xylazine into the heart.

In vitro experiments

Cortical and hippocampal slices were prepared from three of the mice brains. The brains were immediately removed and dipped into cold ($2 - 3$ °C), oxygenated (95% $O_2, 5\%$ CO_2) cutting solution. The cutting solution contained the following composition (in mM): 250 Sucrose, 26 $NaHCO_3$, 10 D-Glucose, 1 KCl, 1 $CaCl_2$ and 10 $MgCl_2$. 500 μm thick horizontal slices were cut by a vibratome (VT1200s; Leica, Nussloch, Germany) from both hemispheres. Slices were kept in a standard artificial cerebrospinal fluid (aCSF) solution at room temperature ($20 - 22$ °C) for at least one hour before use. The recordings were performed at $32 - 34$ °C with a standard recording aCSF containing (in mM): 124 NaCl, 26 $NaHCO_3$, 10 *D*-Glucose, 4 KCl, 2 $CaCl_2$ and 2 $MgCl_2$. In the recording chamber, a dual-perfusion system was used by perfusing both the top and the bottom surfaces of the slices with relatively high perfusion speed (> 10 ml/min) to provide better oxygenation, similar to *in vivo* conditions [140].

In vivo experiments

The anesthetized mice were stabilized in a stereotaxic frame (David Kopf Instruments, Los Angeles, USA) so as to make their skull fixed during the experiments. Craniotomy was performed from -1.0 mm to -5.0 mm anteroposterior (AP), from 1.0 mm to 4.0 mm mediolateral (ML) in reference to the Bregma of two GCaMP6 mice. In case of perpendicular implantation the silicon based MEA is proved to be rigid enough to penetrate into the dura mater, but during our experiments the shanks of the self developed MEA included an angle of 20 degree relative to the surface of the brain, thus in order to achieve a smooth implantation by avoiding possible buckling of the probe, the dura mater was incised above the target location. The target area was located typically in the middle of the CW, depending on the topology of the veins on the surface of the exposed brain. With the applied MEA and the angle we were able to reach the somatosensory cortex of the brain, which was suitable for the two-photon imaging too.

3.1.2 Two-photon imaging

The three dimensional observation of morphology was performed with two-photon microscope (Femtonics Ltd., Budapest, Hungary) with the application of an XLUMPLFLN20XW fluid immersed objective (Olympus Corporation, Tokyo, Japan). The working distance of the objective was 2 *mm* with the magnification capacity of 20. The two-photon imaging not only let us monitor the neural activity near the applied MEA because of the genetically encoded calcium indicator expressing GCaMP6 cells, but it also made the observation of imaging laser generated artefacts possible. The applied laser was a Chameleon-Ultra II (Coherent Inc., California, USA) high-intensity modelocked Ti:Sapphire laser with the available wavelength tuning range of 680 to 1080 *nm*. During the experiments the best wavelength for the neural imaging was found to be 920 *nm*. The setup was not only able to function in two-photon resonant mode but it also did work in camera mode which allowed us to follow the track of the inserted MEA before and during the insertion because of the built-in charge-coupled device (CCD) camera. With the adequate brain region in the field of view of the two-photon imaging, the bioelectrical activity was monitored in two-photon mode and the electrophysiological measurement setup was assembled.

In vitro experiments

For the optical imaging the prepared slices were placed into an *in vitro* measurement chamber. The chamber ensured the aCSF supplement and circulation for keeping the neural tissue alive until the end of the measurement and it stabilized the slice mechanically with a holder mesh. The top part of the chamber is concave-shaped to hold the aCSF for the liquid immersion objective of the two-photon microscope which was used during the experiments. The schematic of the *in vitro* assembled experiments is shown in Figure 3.1.

In vivo experiments

During the *in vivo* experiments, the mice were held in the stereotaxic frame to keep the examined neural tissue motionless, which is required for the optical imaging. The stereotaxic frame was placed into an *in vivo* measurement chamber. The mice had been anesthetized for the time of the two-photon imaging and the electrophysiological recording. The available space for the MEA implantation was more limited under the field of view of the two-photon microscope than in the the *in vitro* case

as it is shown in Figure 3.2 thus a special designed MEA was required to use for the electrophysiological recordings.

3.1.3 Electrophysiological measurement

The electrophysiological observation of the bioelectrical activity of the examined brain slices and the somatosensory cortex of the living mice were carried out using an Intan RHD 2000 amplifier system (Intan Technologies, Los Angeles, USA) connected to a computer via USB 2.0 with a sampling frequency of 20 kHz. The reference electrode was an Ag/AgCl needle, which was located beneath the tested neural tissue in case of the *in vitro* experiments. During the *in vivo* recordings the reference electrode was inserted under the scalp of the mouse.

In vitro experiments

In case of the *in vitro* electrophysiological recordings a silicon based MEA with 16 shanks (A16x1-2mm-50-177-A16, NeuroNexus, Ann Arbor, MI. USA) was applied as the working electrode. Every shank contained one electrode site at the tip of the

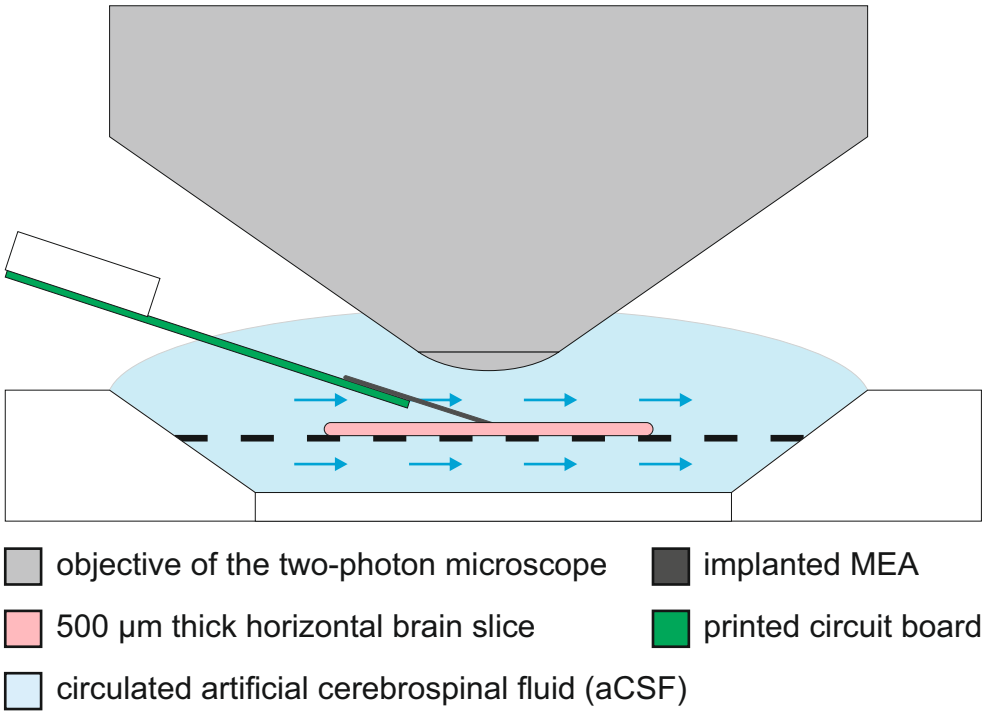

Figure 3.1: *Schematic of the assembled* in vitro *measurement system. In the middle of the* in vitro *two-photon measurement chamber the brain slice is placed on a holder mesh. The chamber provides the aCSF circulation near the neural tissue to keep it bioelectrically active. Under the fluid immersed two-photon objective the applied MEA was inserted into the tissue*

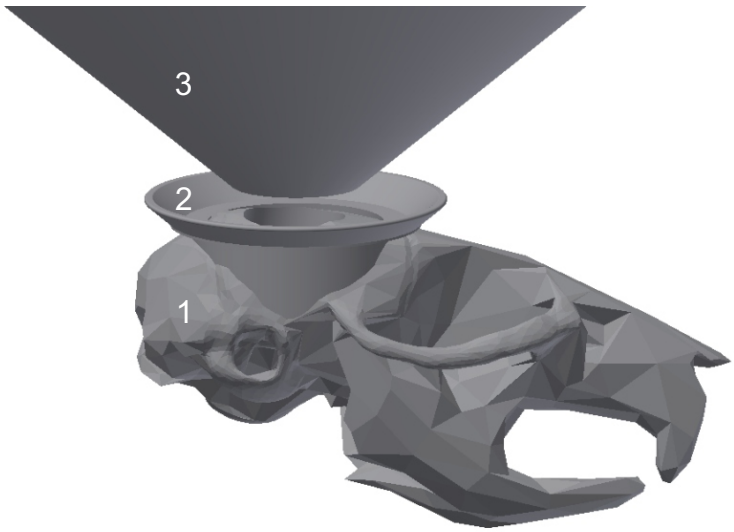

Figure 3.2: *The 3D designed model of the available implantation space during the* in vivo *measurements. A real size mouse skull model (1) was used to observe the required and suitable concave-shaped part (2) for the immersion fluid above the CW and under the objective (3) of the two-photon microscope*

shank for the extracellular recording after the implantation into the brain slice. The geometrical design of the MEA such as the thickness and the length of the shanks or the electrical connectors of the MEA allowed us the insertion into the tissue under the objective of the two-photon microscope [141].

In vivo experiments

Because of the limited implantation space, a special MEA was developed for the *in vivo* simultaneous two-photon imaging and extracellular recording. The MEA is a four-shank (8 channels/shank) silicon based probe assembled with Omnetics electrical connector (Omnetics Connector Corporation, Minneapolis, USA) which small enough to be suitable for further chronic *in vivo* applications too. Between the connector and the silicon part there is a flexible polymer cable which allowed us to implant the probe with a self-designed 3D printed electrode holder. The flexible cable allow the connector to be stabilized somewhere next to the cranial window to the skull without obstructing the two-photon imaging. This is a necessary requirements for further chronic experiments. The stereomicroscopic image of the applied MEA with the flexible polymer cable and the Omnetics connector is shown in Figure 3.3, the schematic of the electrode holder with the flexible cable conducted MEA during implantation is shown in Figure 3.4.

In both cases the MEAs were inserted with the automated electrode holder of the two-photon setup in such a manner that the longitudinal axes of the shanks included

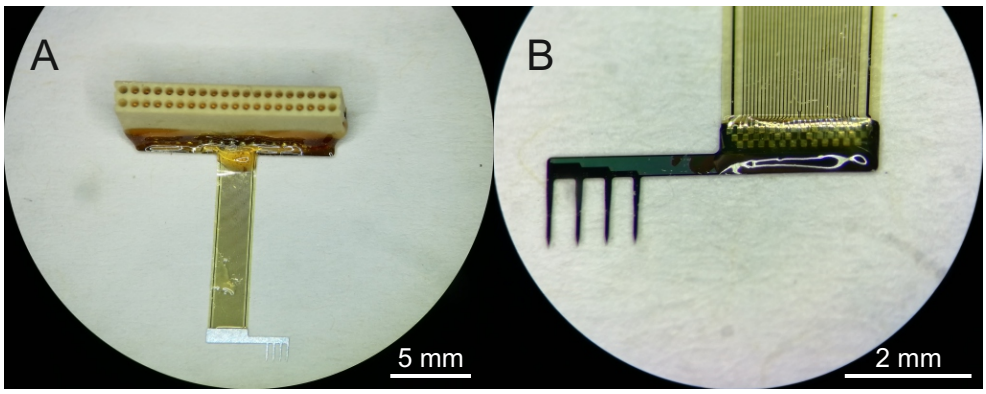

Figure 3.3: *Stereomicroscopic image of the MEA designed for* in vivo *recordings during the two-photon imaging. The Omnetics connector (A) and the four-shank silicon probe (B) are connected with a flexible cable*

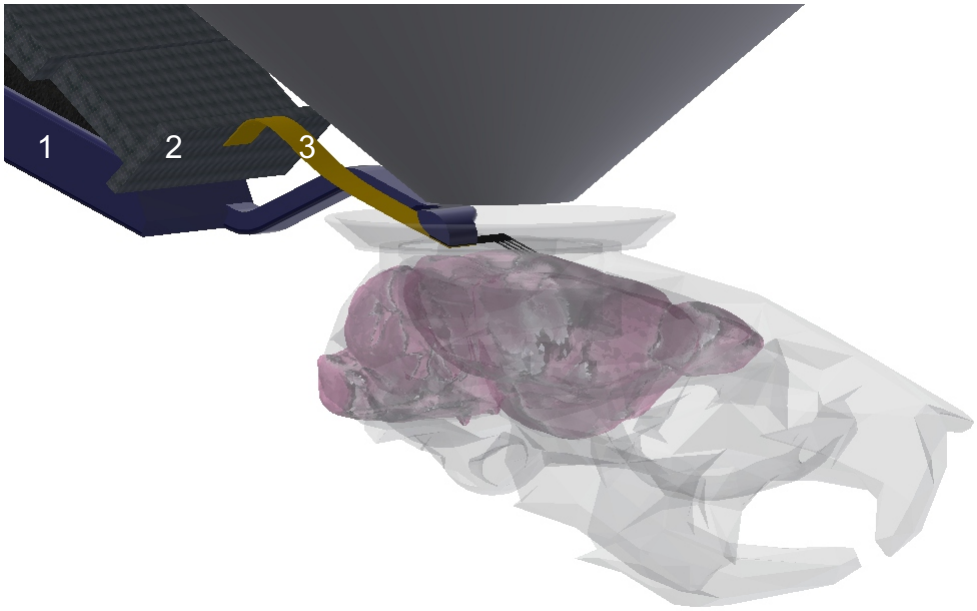

Figure 3.4: *Schematic of the assembled* in vivo *measurement system. The 3D printed electrode holder (1) stabilized the Omnetics connector (2) and the MEA at the end of the flexible cable (3)*

an angle of 20 degree relative to the surface of the brain slice. In case of the *in vitro* MEA, the printed circuit board of the probe was stabilized to the automated electrode holder while during the *in vivo* recordings between the automated electrode holder and the MEA there was a need to apply a 3D printed electrode holder. That holder was designed to be curved to fit in the limited implantation space, and it was glued to the MEA at the connection part of the flexible cable and the silicon probe. The implantation was performed under CCD camera control. After the MEA had reached its final place in the tissue, the two-photon setup was switched from camera mode to two-photon mode and the electrode sites were located. Following this, the focal plane was stabilized and the imaging laser was switched off. The

electrophysiological measurement was started without the laser imaging in order to provide reference recordings. After 8 minutes of such laser-free recordings, the two-photon imaging was initiated and the imaging laser introduced artefacts. Another 8 minutes of laser-noised recordings were hence obtained. The third part of each measurement was performed without the two-photon imaging again, in order to obtain further control data sessions, this time after the laser effect. During the second part of the measurements, the two-photon imaging laser generated artefacts appeared which exceeded the amplitude of SUAs by at least an order of magnitude as shown in Fig 3.5.

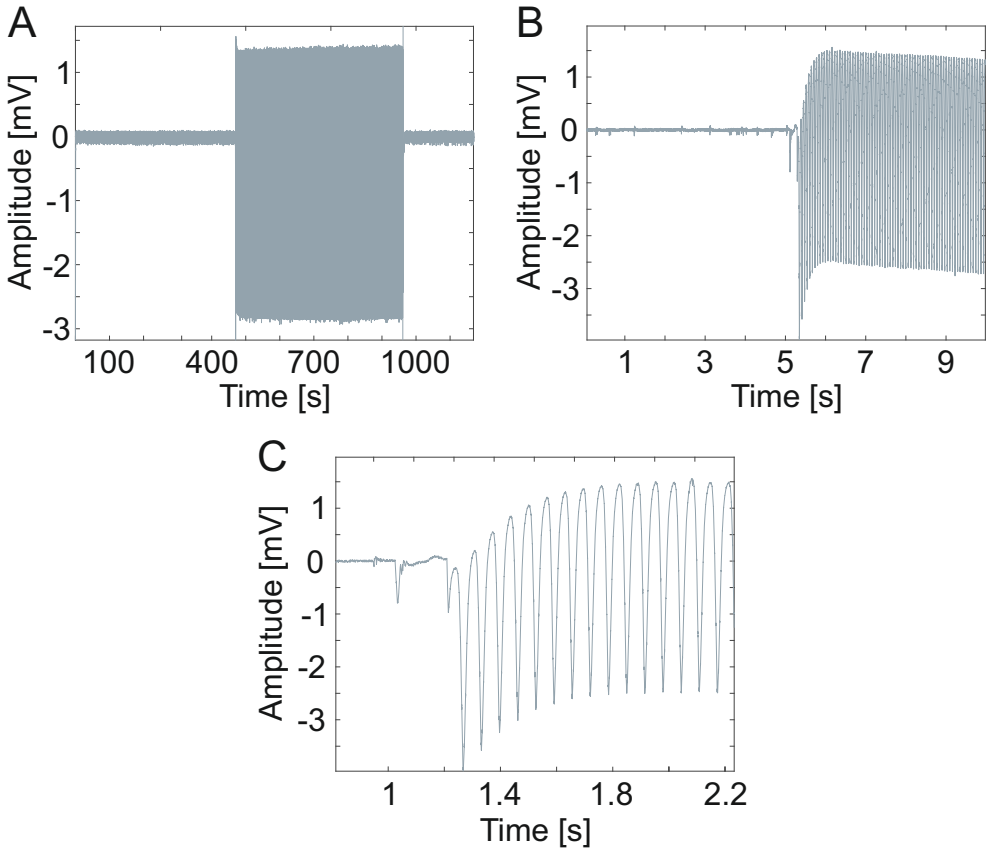

Figure 3.5: *Representative sample of the imaging laser impact on the electrophysiological recordings. Between the first and the last parts of the measurement, which were recorded without two-photon imaging, photoelectric artefacts of the two-photon imaging laser are observable (A). The recorded data at the moment when the imaging laser was switched on (B, C)*

3.1.4 Data analysis

MATLAB 2017a (MathWorks Inc., Natick, MA, USA) was used for off-line signal visualization, filtering and analysis. Figure 3.6 summarizes the steps that had been performed in order to accomplish the identification of spike clusters in the data containing two-photon laser noise.

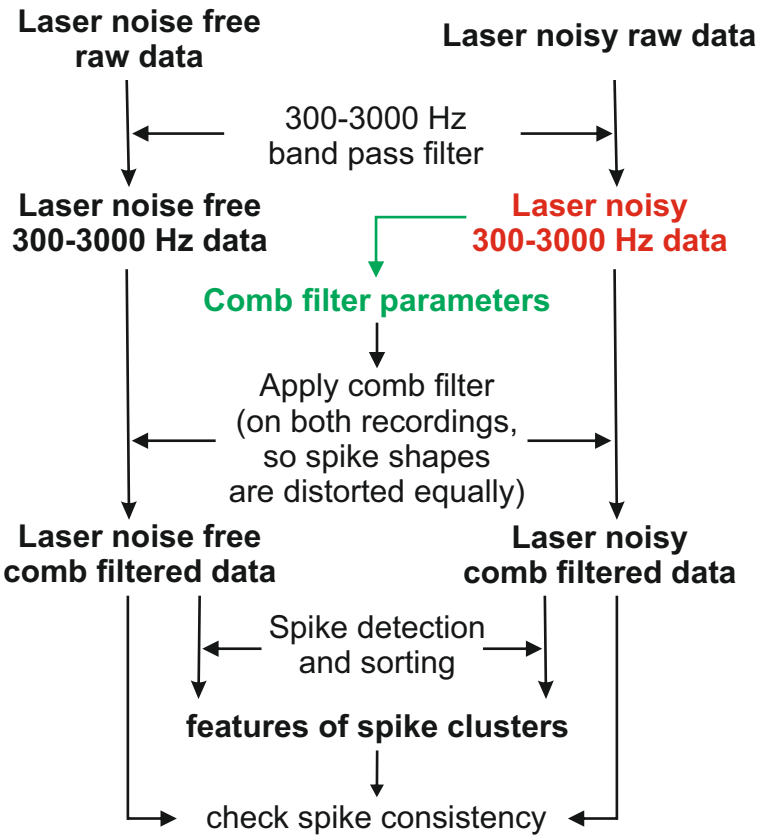

Figure 3.6: *Filtering and analyzing steps. The performed filtering and analyzing steps in order to identify the spike clusters and check the spike consistency between the two-photon imaging laser noise free and the laser noisy data. The green arrow indicate the place of the parameter setting algorithm which is presented in Figure 3.7*

All of the applied band-stop infinite impulse response (IIR) filters were created with passband ripples of 0.4. Since the IIR filters delay some frequency components more the others, they distort the input signals with frequency dependent phase shift. Thus they were applied with the 'filtfilt' Matlab function that compensated the delays introduced by such filters, and thus corrected for filter distortion. The recorded signals were initially filtered with a second order band-pass filter between 300 Hz and 3000 Hz, which is a commonly used method for highlighting and detecting SUAs [142], but not adequate for eliminating the photoelectric artefacts. Following this, Fast Fourier transform (FFT) was applied on the electrophysiological recordings. Comparing the frequency spectra of the first (laser off) part of each measurement to their second part (laser on), it was evident that the imaging laser gave rise to a population of high peaks in the frequency domain. These peaks were located periodically, with a distance of 15.5 Hz between the neighboring ones. This frequency value corresponds to the imaging frame rate of the applied two-photon laser (Figure 3.9). Considering this nature of the artefacts, it is a straightforward idea to utilize of a comb filter algorithm to eliminate the noise of the imaging laser.

The construction process of the laser noise reduction filters is shown in Figure 3.7. Such a comb filter had to be constructed individually for every recording channel because of the different laser noise characteristics on the channels. Each custom-set comb filter was built from filter modules, a representative filter module is shown in Figure 3.8. The modules contain band-stop filters fitted to a certain amount of peaks in the frequency domain.

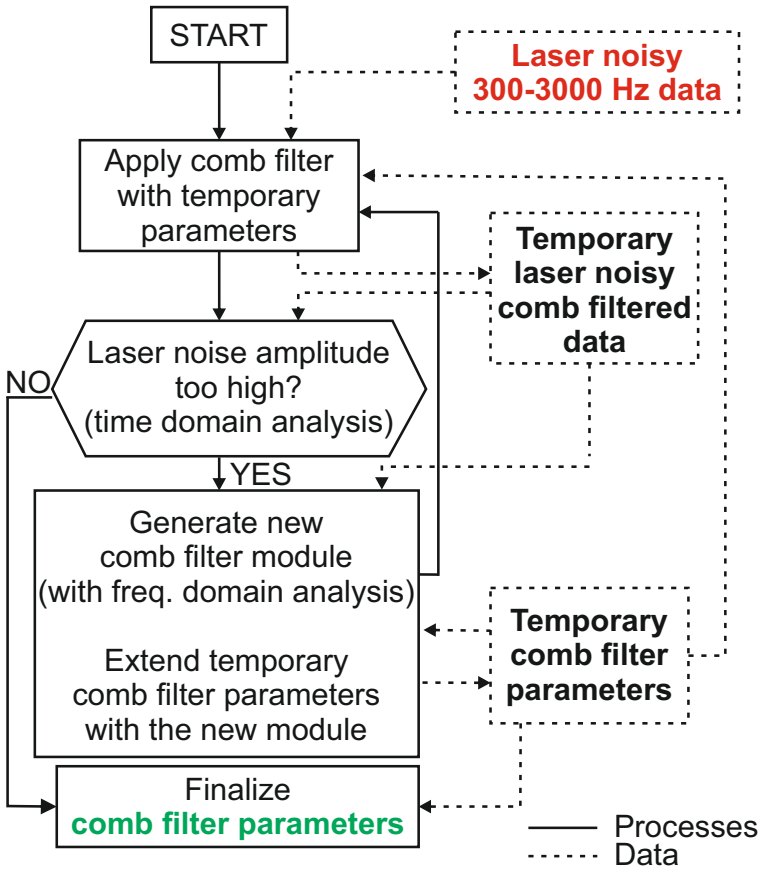

Figure 3.7: *The parameter setting algorithm of the applied custom-set comb filter. The applied parameters are the number of filter modules (N_M), the center frequencies of filter modules (f_{peak}), the number of filters within each module (N_F) and the distance between filters within each module (D_F)*

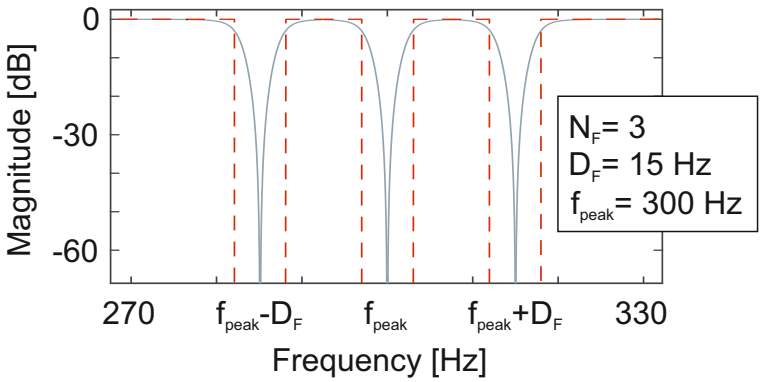

Figure 3.8: *The result of the parameter setting of a representative filter module if $N_M = 1$*

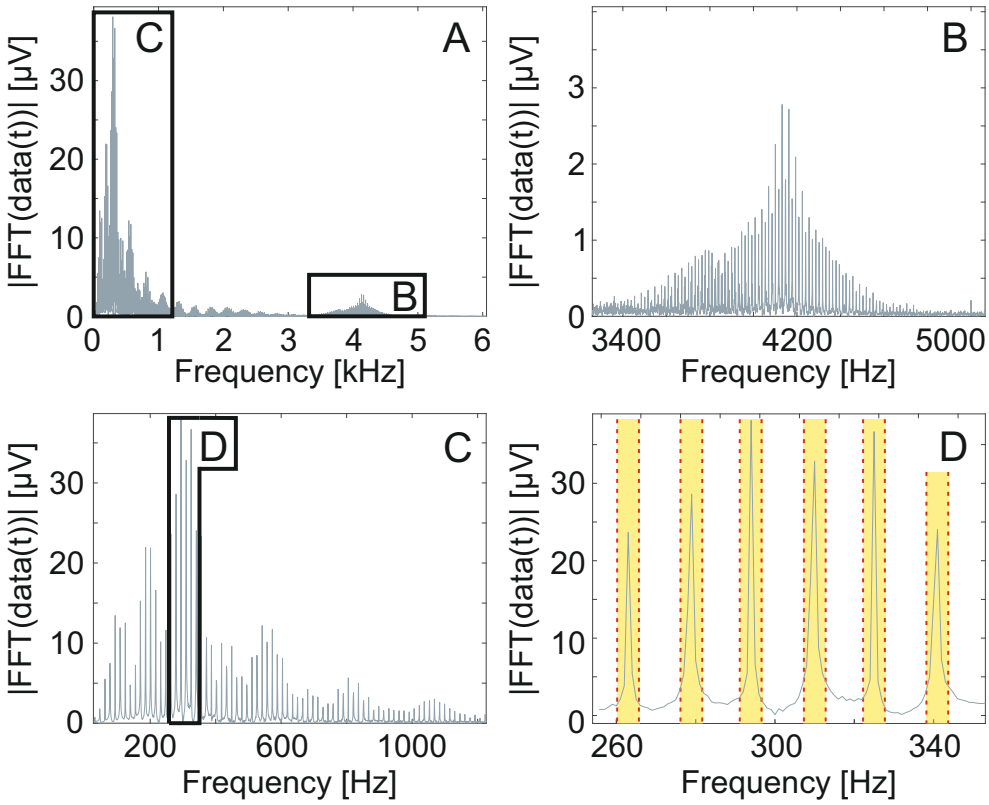

Figure 3.9: *The absolute value of the frequency spectrum of the electrophysiological recordings. The fast Fourier transform analysis of the imaging laser generated noise in the electrophysiological recorded data (A). Harmonics below 1200 Hz (C) and at higher frequencies (B) of the laser generated periodical artefacts appeared with high magnitudes. The overlap of the harmonics is observable (B). A part of the rejected frequencies by the custom-set comb filter is shown in yellow (D)*

The parameter setting algorithm of the comb filter is shown in Figure 3.7. These parameters were the number of filter modules (N_M), a vector containing the center frequencies of the filter modules (f_{peak}), the numbers of the applied band-stop filters within each module (N_F) and the distances between the center frequencies of the applied band-stop filters within each module (D_F). The parameter setting algorithm utilized the $300 - 3000\ Hz$ filtered laser noisy data in a cyclic manner, during each cycle, a new filter module is added to the comb filter. The first step in the cycle was the generation of a temporary laser noise filtered data by the application of the temporary comb filter, i.e. the comb filter generated in the previous cycle on the $300 - 3000\ Hz$ filtered laser noisy data (in the first cycle the number of filter modules is 0, so this step left the data unchanged). The second step was deciding whether the temporary filter was sufficient. This was performed by time domain analysis on the temporary laser noisy filtered data. If the amplitude of the periodic laser noise had been reduced below 40 μV, then the temporary filter parameters became the finalized comb filter parameters. Otherwise, the last step in the cycle followed, which was the generation of a new filter module. This was performed based

on the frequency domain analysis of the temporary laser noisy comb filtered data (which is equivalent to the $300-3000\ Hz$ filtered laser noisy data in the first step). After applying the FFT on this data, the algorithm found the highest peak in the frequency domain. This frequency became the center frequency (f_{peak}) of the new filter module. The neighboring peaks were located at the frequencies of $f_{peakk} \pm nD_F$ (D_F was found to be 15.5 Hz). The values at the neighboring peaks were compared to the highest detected peak to define the number of the applied filters (N_F) within the new module. N_F of the filter module was defined so that the band-stop filters of the comb filter would cover all the neighboring peaks which exceeded in height the 15% of the highest peak (i.e. the one at the center frequency). Every band-stop filter element of the new comb filter module was defined with cutoff frequencies at below 3 Hz and above 3 Hz from the frequency value of each peak. Thus the central rejected frequencies of the comb filter were adjusted to the frequencies of the laser noise peaks and each section of the comb filter had a 6 Hz wide rejected band, as shown in Figure 3.8 and in Figure 3.9.D. The temporary comb filter was extended with the thus obtained new module and the cycle restarted. This process was repeated until the time domain analysis gave positive result, i.e. the amplitude of the laser noise peaks in the time domain became lower than 40 μV, in which case the summarized comb filter parameters were accepted. The thus constructed comb filters were applied on both the laser noise free and the laser noisy $300-3000\ Hz$ filtered data in order to equally distort the SUA (i.e. spike) waveforms in both cases. Later on, this allowed us to match the features of different spike clusters in the laser free and laser noisy measurements. Since the imaging laser generated artefacts were nonuniform along the electrodes, recordings from different electrodes required filters with custom-set parameters. We investigated whether the comb filter prevents us from SUA detection and sorting. Spike detection was performed by simple thresholding. Three features of each potential spikes were defined for spike sorting, which were the location of the minimum amplitude value of the spike, and the values at 250 μs (i.e. five datapoints at 20 kHz sampling frequency) before and after the peaks as shown in Figure 3.10.

The clusters were manually accepted or discarded based on spike waveforms and autocorrelograms. This feature extraction method was preferred rather than the most commonly used method for spike sorting, the principal component analysis (PCA) [143], because the thus defined features could provide more robust information about spike waveform consistency (spike stability). In terms of the laser noise free part of the experiments, I performed a comparison of the feature-based and the PCA methods on the band-pass filtered data to verify the results of the feature extraction based method which was used for testing the spike stability too. Having

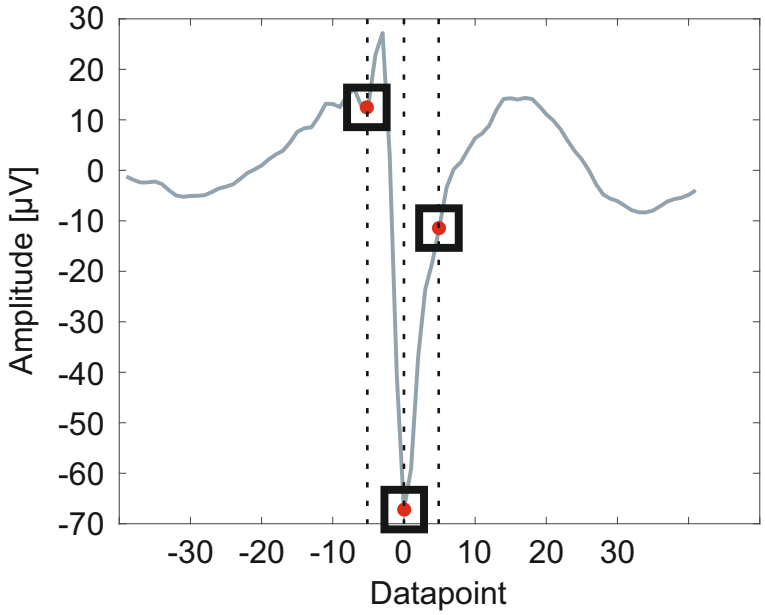

Figure 3.10: *The applied principal component selection. Each potential spike was defined with their three principal component before spike sorting: the location of the minimum amplitude value of the spike, and the fifth datapoints before and after the peak*

applied the commonly used $300 - 3000\ Hz$ band-pass filter on the laser noise free data, spike sorting was performed based on PCA then the results of the PCA based and the feature extraction based sorting process were compared. I have performed a comparison on the sorted spike waveforms and on the interspike intervals too. Interspike interval validation is a commonly used method for checking the quality of MEA performance over a longer period of time [143].

The spike stability was verified as follows. First, the averages and the standard errors of the means of each feature were calculated in every minute of the recordings. These values were compared to each other during the whole measurement to verify the impact of the imaging laser and the applied filters to the shape of the thus sorted spikes. Furthermore, the number of spikes were counted in every minute of the recordings for each clusters. This method showed whether the artefacts caused by the imaging laser gave rise to false positive SUA detections. Another examination of the possible false positive SUA detection was the comparison of the detected spike waveforms and an autocorrelogram belonging to a specific SUA during the laser noisy and the laser noise free recording. With the inspection of the waveforms and the autocorrelograms during the laser on and the laser off sections I could check the effect of the imaging laser on the neural cells firing. To be convinced that the periodic imaging laser did not generate false positive spikes when the period reach the electrode of the MEA, I observed the average occurrence of the sorted spikes within the laser noise contaminated period.

3.2 Materials and methods related to the determination of the thickness dependent electrical impedance spectrum of human dentin

3.2.1 Specimen preparation

Dentin disks were prepared from human wisdom teeth for the *in vitro* characterization of the thickness dependent impedance of human dentin. Five teeth were removed without damage in the Semmelweis University, Department in Community Dentistry. The collection and application of the specimens happened anonymously in accordance with the research ethical approval made by the Semmelweis University Regional Scientific and Research Ethics Committee with the permission note of 246/2017. The protocol of specimen preparation was the following. The roots were stabilized in dental gypsum and with a suitable saw (Hofer, Aathal - Seegräben, Switzerland) from 1 mm to 2.3 mm thick dentin disks were cut from the occlusal surface of the crown between the pulp and the enamel. The thickness of a prepared disk was depending on the extension of the intact volume of the examined tooth. The surfaces of the prepared disks were cleaned with 35% phosphoric acid for 20 seconds long to open the dentinal tubules from smear layer. The specimens were stored in 0.154 mol/L sodium chloride solution. A representative sample of the prepared dentin disks is shown in Figure 3.11 subfigure A.

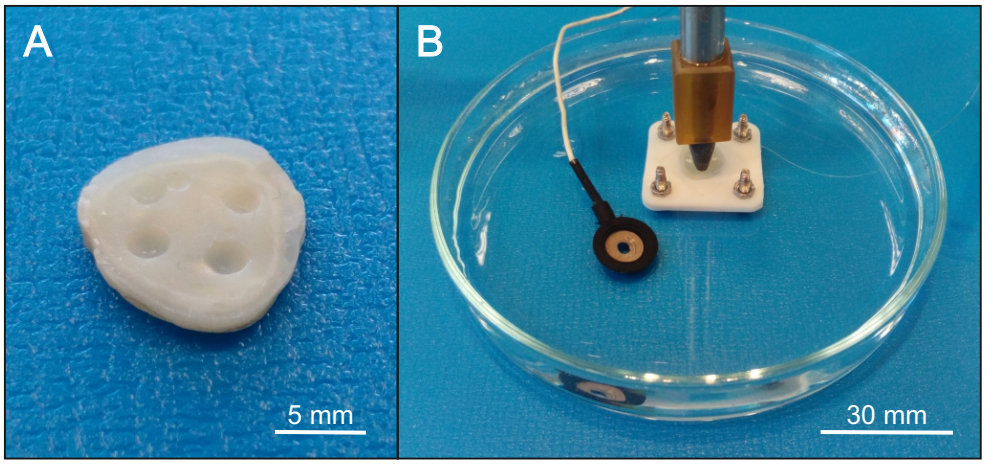

Figure 3.11: *A representative sample of the prepared dentin disks with four test areas after the drilling processes (A) and during the impedance measurement in the Petri dish with the reference electrode next to the dentin disk holder (B)*

3.2.2 Thickness measurements

Prior to realizing thickness measurements, $3-4$ separated test areas had been specified on the surface of each dentin disk. The number of the specified areas depended on the size of the intact area of the examined dentin disks. A layer thickness measurement apparatus was applied on the middle of the defined test areas. The accuracy of the thickness measurement method is critical for proper calculation of the thickness dependency of the impedance, thus a stereotaxic frame with 10 μm resolution (David Kopf Instruments, Los Angeles, USA) was used for this purpose. A needle was fastened to the electrode holder of the stereotaxic frame. Using a microscope, the reference thickness value was defined where the needle point reached the surface of the frame. The examined dentin disk was placed under the lifted needle to measure the thickness of each test area. Following this, the thickness values of the test areas were calculated by subtracting the reference values from the thickness values which were measured on the top of the test areas. The thickness measurement method was utilized before every impedance measurement to specify the correlation between the thickness and the impedance of the dentin.

3.2.3 Impedance measurement system

An Intan RHD 2000 amplifier system (Intan Technologies, Los Angeles, USA) was used for impedance measurements. The system contained an Intan RHD 2000 USB interface board with a 16-channel amplifier board. The amplifier board was connected to the interface board via an SPI interface cable, the interface board was connected to a computer via USB 2.0. One of the sixteen channels was used to measure the impedance between the reference electrode and the working electrode. During the experiments the reference electrode was an Ag/AgCl electrode and the working electrode was an 80% Pt $-$ 20% Ir 40.46 μm thick micro wire (California FineWire Company, California, USA). The experiments were performed in 0.154 mol/L NaCl solution. The examined dentin disk was placed in a holder in a Petri dish filled with the said NaCl solution. The holder allowed the solution to flow under the specimen and through the dental tubules. The reference electrode was inserted in the solution near the specimen while the working electrode was built into a silicone tube. The inner diameter of the applied tube was 1 mm so the measured dentin surface was 0.785 mm^2. The silicone tube was also filled with the NaCl solution and it was gently pressed to the dentin to insulate the working electrode from the surrounding solution. Because of the insulation, the ion current between the working and the reference electrode could only flow through the dental tubules during the impedance

measurement. The thus assembled measurement system is shown in Figure 3.11 subfigure B and the schematic of the assembled system is presented in Figure 3.12.

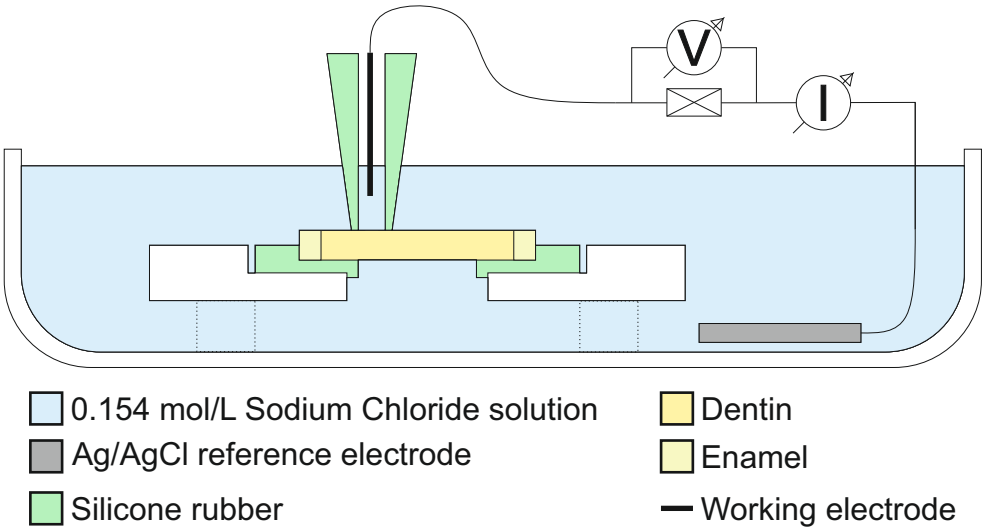

Figure 3.12: *The schematic of the assembled impedance measurement system. The electric circuit between the working electrode and the reference electrode can only be closed through the dentin tubules because of the insulator silicones*

3.2.4 Impedance measurement

The insulation of the silicone tube was verified before the impedance measurements of the test areas. The filled tube with the working electrode in it was gently pressed to the bottom of the Petri dish. The reference electrode was next to the tube as we described it earlier. The impedance measurement system has shown that there was no electrical connection between the two electrodes so the insulation of the silicone tube was suitable for the further recordings. Prior to measuring the impedance of the dentin disks it was necessary to define the impedance of the working electrode and the transfer fluid to calibrate the measurement system. The thus defined electrode impedance was subtracted from the impedance values measured on test areas to get the impedance of the examined dentin. After every thickness measurement the impedance of each test area was measured at multiple frequencies between 50 Hz and 5000 Hz and the coherent thickness-impedance values got recorded according to the frequency. As the next step of the measurement process, test areas of dentin disks were thinned with low speed dental drill. After thinning the same cleaning method was performed with phosphoric acid which was utilized after cutting dentin disks. The cleaning was followed by thickness measurement and the specimens were immersed to the NaCl solution to refill the dental tubules with saline. As it was done, the impedances of thicker test areas were measured and the new thickness-

impedance values got recorded. The whole measurement process was repeated until the dentin disks were reduced to a thickness of 0.3 mm.

3.2.5 Data analysis

The first step of the data analysis was to compare the corresponding thickness and impedance values. Following that, focus groups were organized based on the measured thickness to observe the impedance of thickness ranges. Group intervals were defined with consideration of the importance of the remaining dentin thickness in clinical practice. The thus defined focus groups and their quantity of samples are shown in Table 3.1.

Group No.	**Max thickness**	**Min thickness**	**Quantity of samples**
6	2.28 mm	1.25 mm	13
5	1.24 mm	0.95 mm	14
4	0.94 mm	0.75 mm	9
3	0.74 mm	0.60 mm	13
2	0.59 mm	0.45 mm	11
1	0.44 mm	0.30 mm	11

Table 3.1: *Quantities and ranges of focus groups of the recorded thickness-impedance pairs for data analysis*

For statistical analyzing IBM SPSS Statistics 24 (IBM Corporation, New York, USA) software was used. The focus groups were observed by Kruskal - Wallis test on $p = 0.002$ significance level, and by using LSD as a post hoc test.

Chapter 4

Results and Discussion

4.1 Results concerning the simultaneous electrophysiological recording and two-photon imaging

As detailed in section 1.2.1, simultaneous two-photon imaging and electrophysiological measurements with MEMS technology based microelectrode arrays at the same location is compromised by the formation of photoelectric artefacts in the electrophysiological signals. Regarding our experiments when electrodes were located within the field of view of the two-photon microscope, the imaging laser was able to create such artefacts with amplitudes of typically 50 times greater than the amplitude of the largest SUAs. Moreover, the complicated spectrum of the photoelectric noise prevents the filtering of the artefact with the application of simple filters. Our following results suggest that the utilization of a comb filter based algorithm can enable researchers to detect and sort SUAs even if the tissue surrounding the MEA is observed with two-photon microscopy.

Since the filtering and analyzing steps of the custom-set comb filter based algorithms were based on the same ideas in case of the *in vitro* and in the *in vivo* experiments, the results of the self-developed filtering and analyzing algorithm for simultaneous experiments of electrophysiology and two-photon imaging are going to be presented just in case of the *in vitro* experiments in detail. Representative results of the filtering and analyzing process from the *in vivo* recordings during two-photon imaging will be presented afterwards then the discussion on the results will be reviewed at once in case of the *in vitro* and the *in vivo* experiments.

4.1.1 Results concerning the simultaneous *in vitro* experiments

Figure 4.1 illustrates the observed area in case of the *in vitro* experiments and suggests that the above described two-photon microscope setup and settings were suitable for detecting activities of neuron somas and dendrites via calcium imaging. The green charts above the highlighted squares show the calcium imaging intensity during a session of two-photon imaging, where the peaks indicate the bioelectrical activity of the GCaMP6 neural tissue.

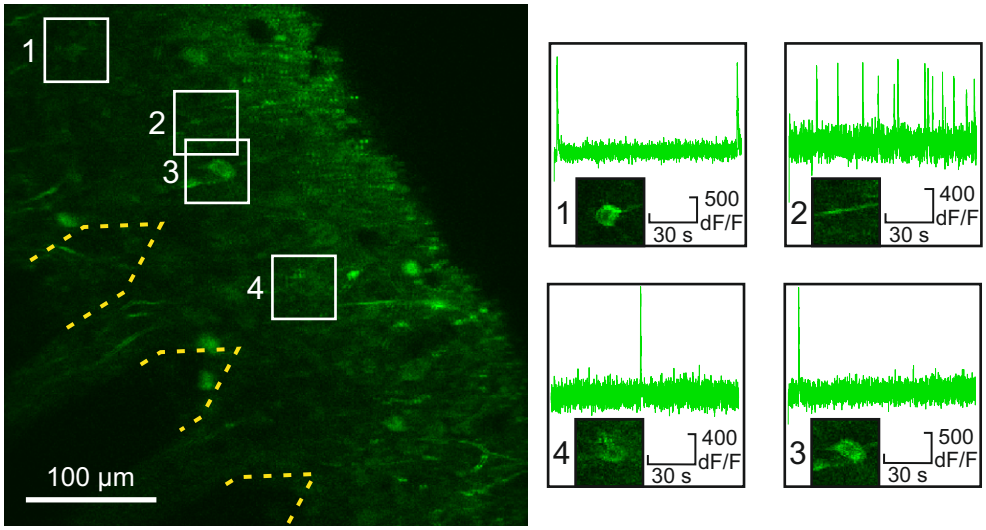

Figure 4.1: *Two-photon calcium imaging. The imaging reveals activities of neuron somas (subfigures 1, 3, 4) and dendrites (subfigure 2) in the vicinity of the microelectrode array*

The filters influenced frequency spectrum of the electrophysiological recordings is shown in Figure 4.2, where subfigure A shows the absolute value of the frequency spectrum of the unfiltered signal, subfigure B shows the absolute value of the frequency spectrum of the band-pass filtered signal while subfigure C shows the absolute value of the frequency spectrum of the band-pass and noise filtered signal. Comparing the subfigures, it can be observed that after both of the filtering processes the frequency component of the noise became two orders of magnitude lower.

Figure 4.3 shows neural signal samples obtained from an electrode illuminated with direct laser light before (gray) and after (orange) the application of the complex comb filter based filtering algorithm. It is evident that small amplitude spike-like artefacts are still present on the filtered signal and these spike-like artefacts are synchronized with the period of the laser noise. Fortunately, however, we can also observe that major single unit activity amplitudes exceed the amplitude of these artefacts. The filter was also applied on the signal sections which were recorded when the imaging laser was off so those sections can serve as proper references for

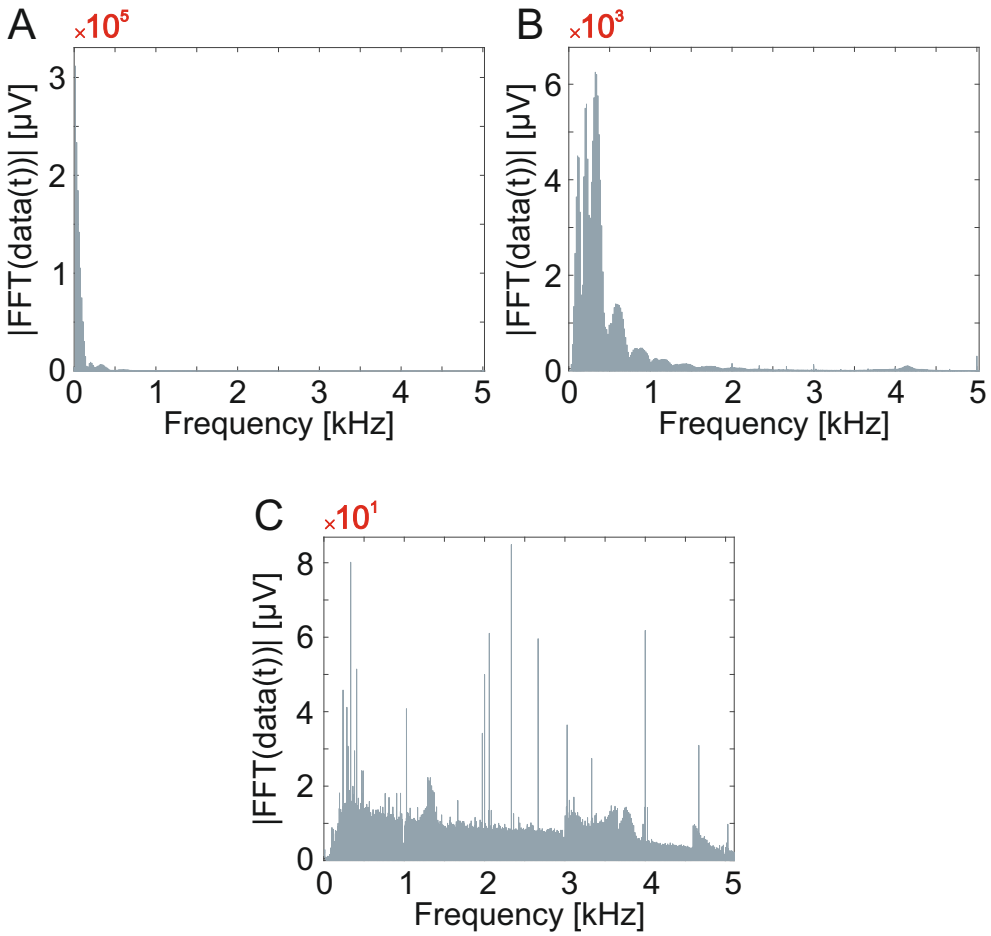

Figure 4.2: *The filters influenced frequency spectrum of the electrophysiological recordings. Subfigure A shows the absolute value of the frequency spectrum of the unfiltered signal, subfigure B shows the absolute value of the frequency spectrum of the band-pass filtered signal and subfigure C shows the absolute value of the frequency spectrum of the band-pass and noise filtered signal*

single unit activity detection. Moreover, with further developments, the artefact spikes can probably be eliminated with an algorithm which takes into account the synchrony of the artefacts and the laser noise. A limitation of this proposed method is that when a single unit activity coincides with a spike artefact, it is probably also eliminated. However, comparing the width and the density of the laser generated artefacts in time range, this limitation should only affect approximately 8.5% of the signal.

Figure 4.4 shows one of the tissue region observed with two-photon microscopy, containing the recording electrode sites. The Figure 4.4 shows the recording position from where the representative detected and sorted SUA, which will be presented in the following, was recorded. The result of the feature extraction for this representative case is shown in Figure 4.5, where the potential spikes are shown in black if they were detected during the laser off condition, and red if they were detected during the laser on condition.

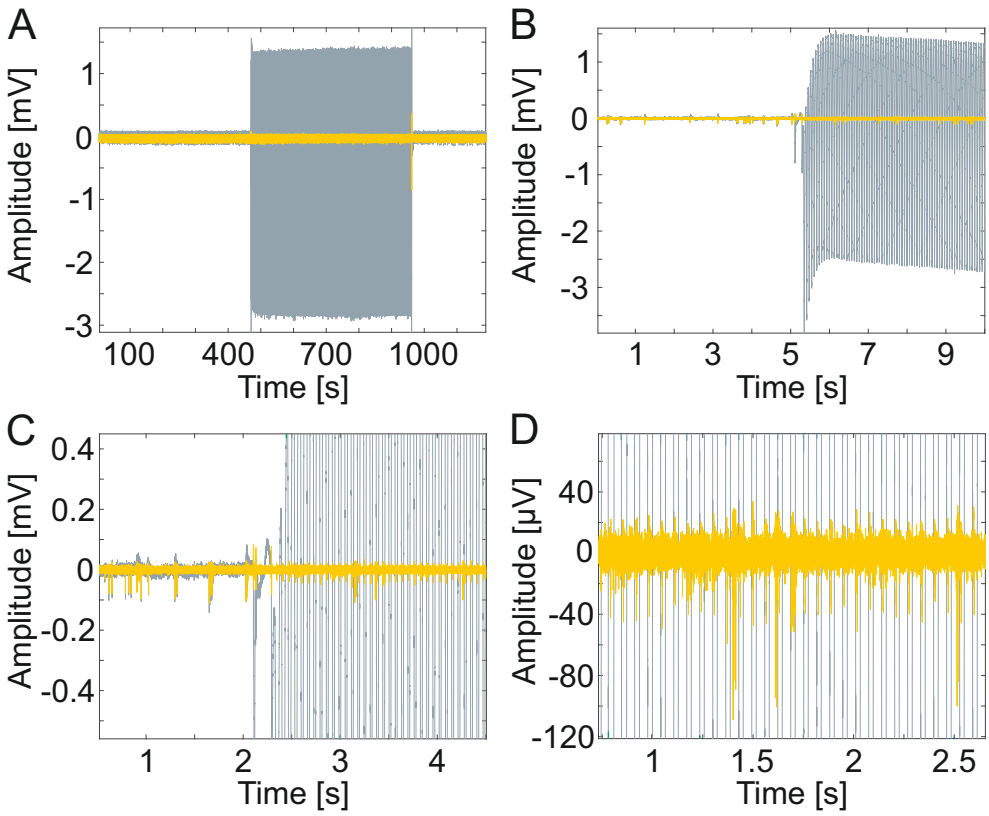

Figure 4.3: *Representative sample of the results of the applied filtering algorithm. The subfigures show the same data as Figure 3.5 does, prior to filtering (gray) and after applying the filtering algorithm (orange)*

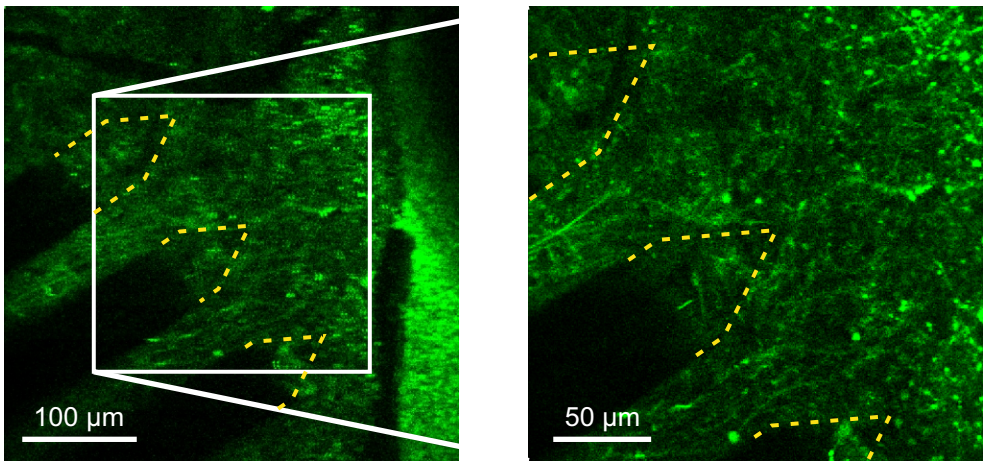

Figure 4.4: *Two-photon image from the simultaneous electrophysiological recording and two-photon imaging with the applied MEA inserted into the neural tissue in the field of view of the two-photon microscope*

The obtained spike waveforms and their average are presented in Figure 4.6 subfigure A, the associated autocorrelogram is presented in Figure 4.6 subfigure B.

To verify the applied filtering algorithm, the consistency of the sorted spike waveforms (spike stability) was visualized. Results of the average of spike features within each minute of the recordings suggest that the laser noise does not corrupt the thus

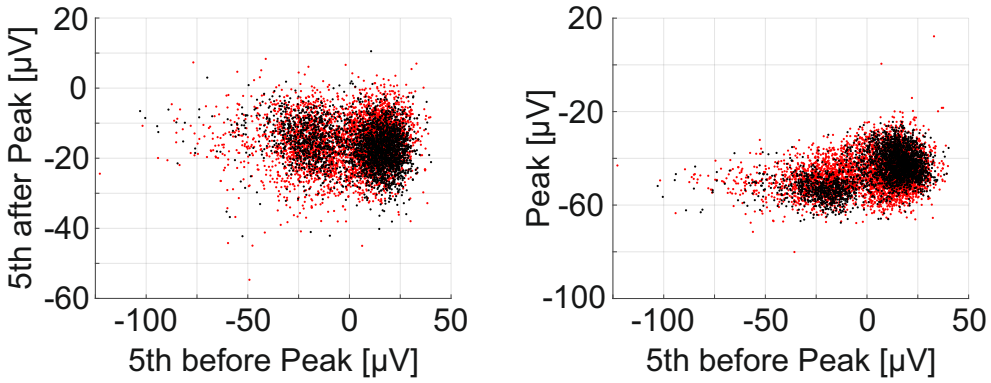

Figure 4.5: *Potential spikes were sorted using three features obtained from the comb-filtered signals. Every dot shows a feature of a detected potential spike. The black dots belong to spikes from the laser off part, the red dots belong to spikes from the laser on part of the presented experiment*

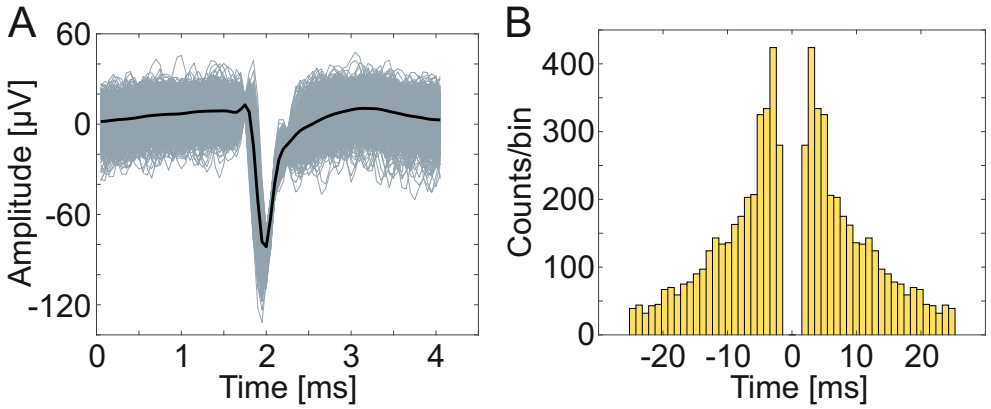

Figure 4.6: *The obtained spike waveforms (A) and their average (black line) and the autocorrelogram of the thus sorted spike (B)*

obtained spike waveforms. The averaged feature components within the measuring minutes is shown in Figure 4.7 subfigure A. The slight decrease of the amplitude feature (shown in orange) could be caused by the nature of the long term experiments of brain slices. The number of the detected spikes within every minute of the measurement is shown in Figure 4.7, subfigure B. The result of the subfigure probably did not indicate false positive SUA detection, it rather suggested that the imaging laser may had effect on the neural cells firing rates. To verify this statement, I observed the differences between the laser on and the laser off conditions from multiple angles.

The differences between the first laser off and the laser on conditions are observed in terms of the spike waveforms and their averages in Figure 4.8, where the subfigure A presents the first laser off condition, the subfigure B presents the laser on condition and subfigure C presents the differences in the averages of the observed waveforms. The slight decrease in the amplitude of the sorted SUA can be observed during the laser on condition as it was shown in Figure 4.7 subfigure A, but the sorted

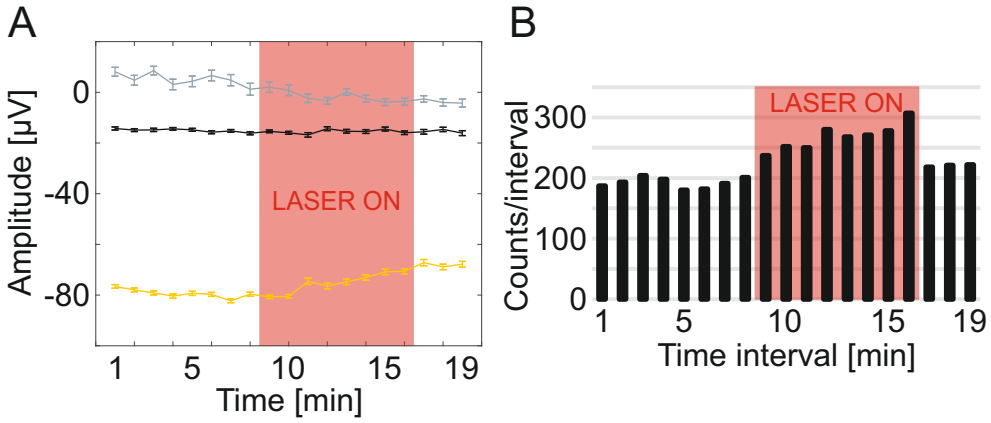

Figure 4.7: *Spike stability observation. The averaged feature components (A) and the number of the detected spikes (B) within every measuring minutes*

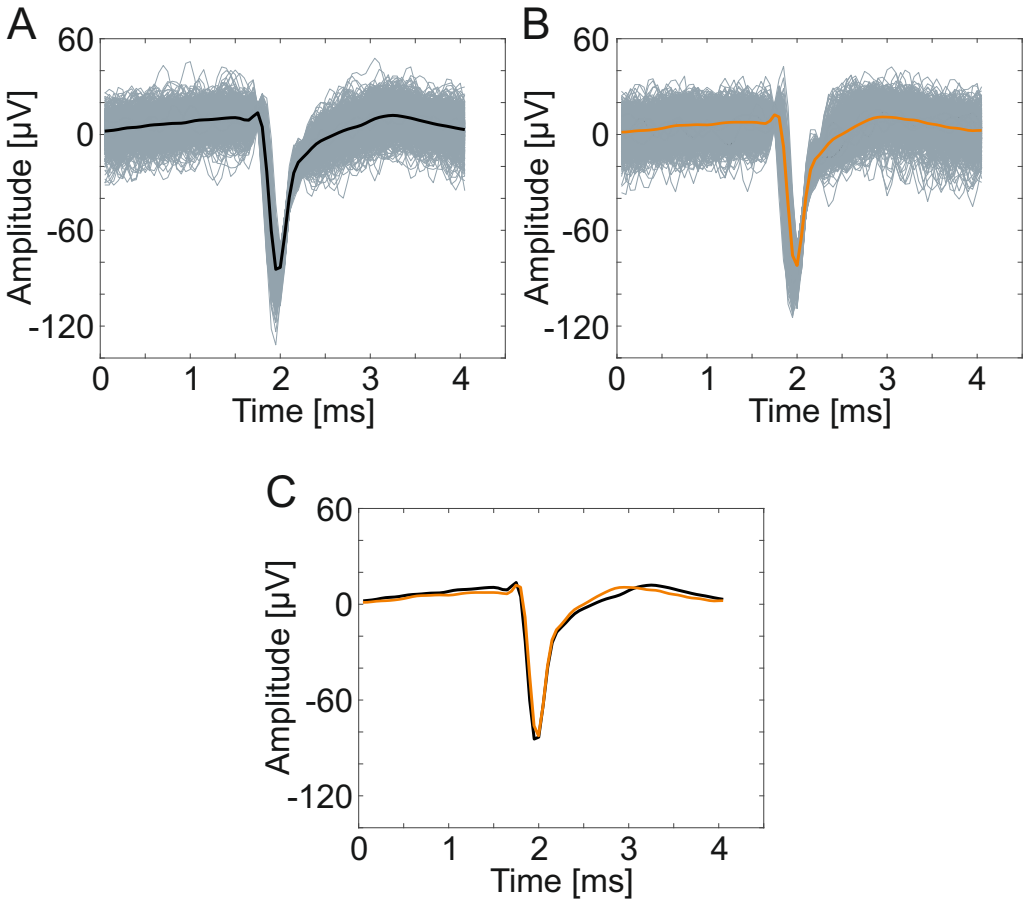

Figure 4.8: *The differences in spike waveforms and their averages between the first laser off (A, average is black), the laser on (B, average is orange) conditions and the comparison of the averages (C)*

waveforms and their averages show similarity. To verify that the waveforms belonged to one single unit, their autocorrelogram were compared during the first laser off and the laser on conditions. The associated autocorrelograms are shown in Figure 4.9 where the subfigure A presents the first laser off condition and the subfigure B presents the laser on condition. The nature of both autocorrelograms indicate that

the observed spikes came from the same single neural cell, moreover the increased number of spikes which was identified in Figure 4.7 subfigure B can be observed in the autocorrelogram in the laser on condition too.

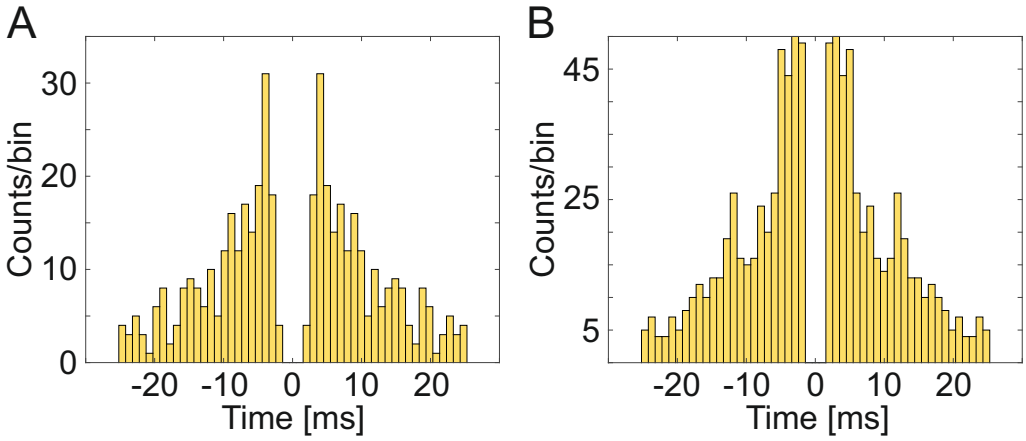

Figure 4.9: *The differences in the autocorrelograms between the first laser off and the laser on conditions*

This result may be caused by modulations of the cells firing rates due to the laser light, as suggested by Kozai et al [144]. This statement is might be confirmed by the histogram of the occurrence of the presented spike within the laser noisy period, which is shown in Figure 4.10. The width of a noisy period, which is the distance between two neighboring laser generated artefact peaks, is equal to 15.5 Hz or 64.52 ms as it can be observed in Figure 4.10. The average occurrence of the presented spike within the laser noisy period seems to be increased.

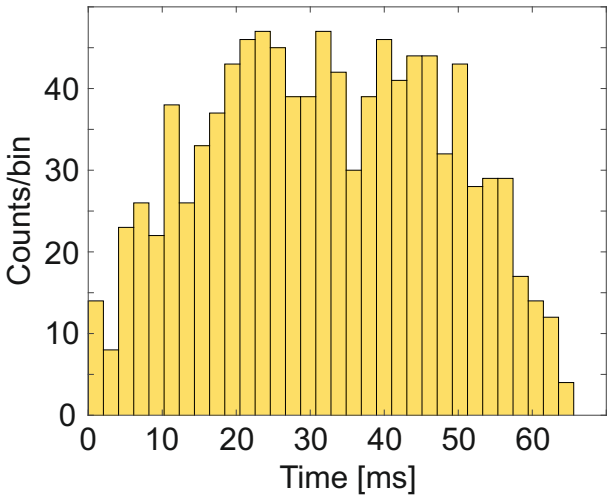

Figure 4.10: *The histogram of the average occurrence of each spike within the laser noisy period*

The results of the comparison of the above described special feature extraction and the PCA based methods for spike sorting is shown in Figure 4.11, in Figure 4.12 and in Figure 4.13. The comparison was performed on the first laser off period of

the experiments, on the same recordings which were presented above. Figure 4.11 presents the first, the second and the third principal components of the PCA of the $300-3000\ Hz$ band-pass filtered laser noise free data. Having applied the feature extraction method on the same $300-3000\ Hz$ band-pass filtered laser noise free data, the results of the spike sorting and clustering method is presented in Figure 4.12, where subfigure A presents the spike waveforms of a cluster and their average based on PCA, and subfigure B shows the spike waveforms of the same cluster and their average based on the special feature extraction method. The clustering was performed manually after the spike sorting process. The results of the interspike interval analysis is presented in Figure 4.13, where subfigure A shows the interspike intervals of the SUAs based on PCA, and subfigure B presents the interspike intervals of the SUAs based on the special feature extraction method. The two different spike sorting methods provide similar results. As it is shown in Figure 4.12, the averages of the clustered spike waveforms based on the PCA and the feature extraction methods indicate that the spike sorting provided the opportunity to cluster the same SUA from the $300-3000\ Hz$ band-pass filtered laser noise free data. The nature of the interspike intervals shown in Figure 4.13 presents similarity, the slight differences in the number of the spikes might come from the manual clustering process.

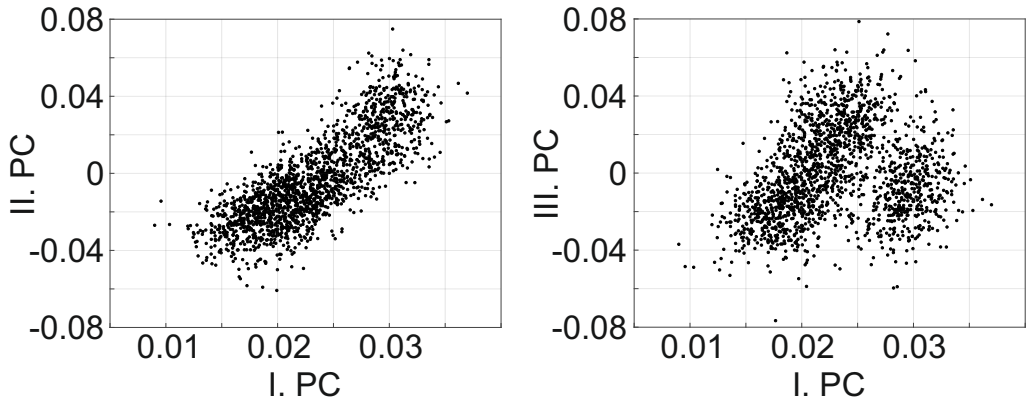

Figure 4.11: *The first, the second and the third principal components of the PCA of the* $300-3000\ Hz$ *band-pass filtered laser noise free data for the comparison of the feature extraction and the PCA based methods for spike sorting*

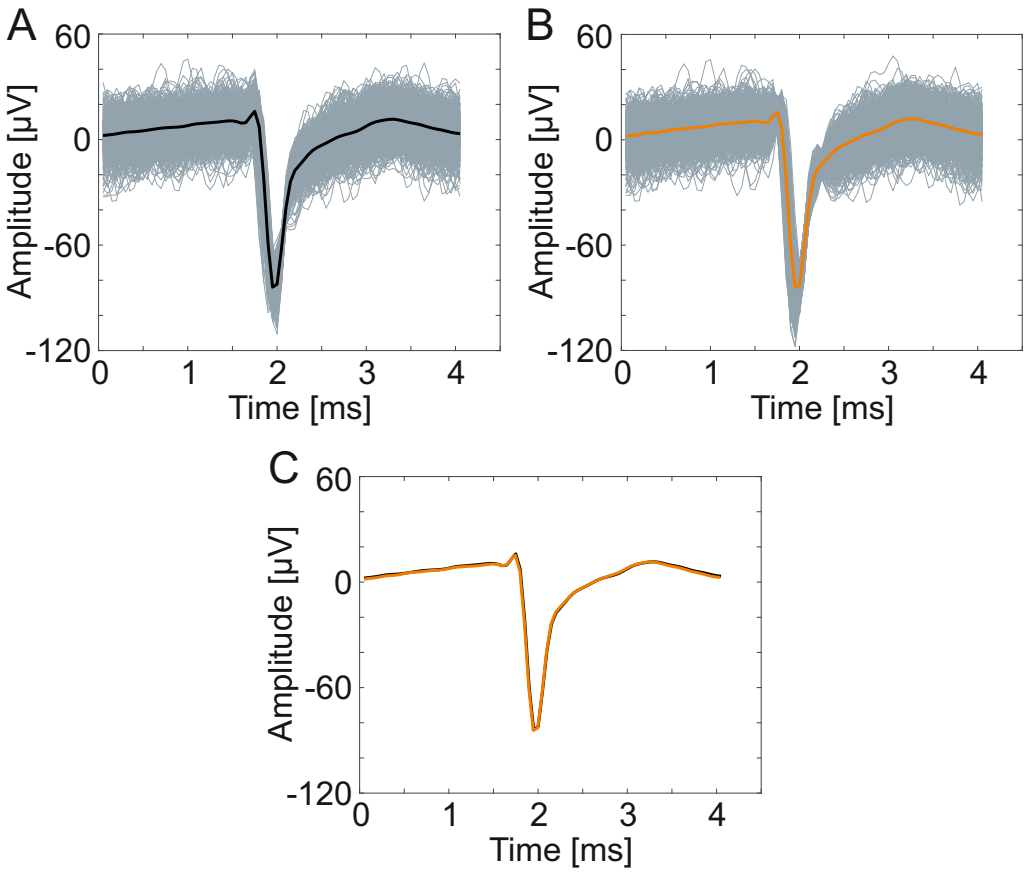

Figure 4.12: *The comparison of the feature extraction and the PCA based methods for spike sorting. The spike waveforms and their average (black line) of a cluster based on PCA (A), and the spike waveforms and their average (orange line) based on the feature extraction method (B). The comparison of the averages (C)*

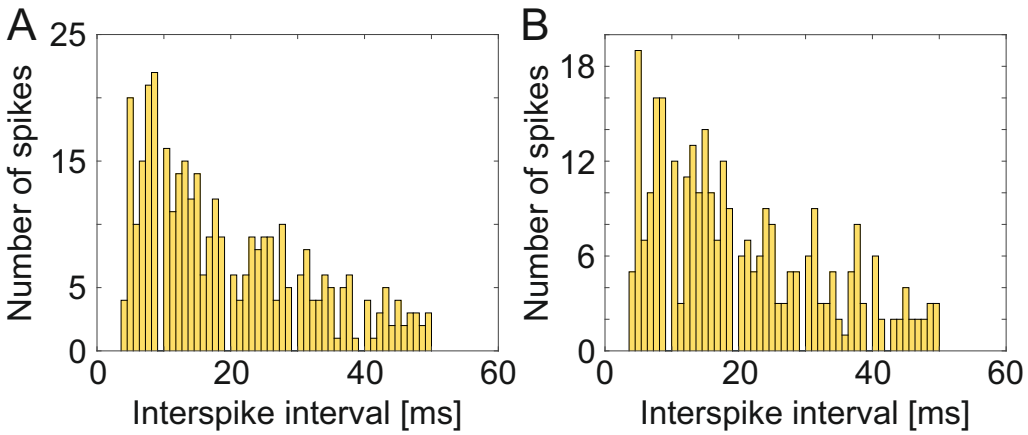

Figure 4.13: *The comparison of the feature extraction and the PCA based methods for spike sorting. The interspike intervals of a SUA cluster based on PCA (A), and the interspike intervals of the corresponding SUA cluster based on the feature extraction method (B)*

4.1.2 Results concerning the simultaneous *in vivo* experiments

To prove that the developed MEA was suitable for electrophysiological *in vivo* recording during two-photon imaging, we performed acute *in vivo* experiments on mice. After the insertion of the MEA inside the CW of the mice skulls, we accomplished calcium imaging as it is illustrated in Figure 4.14. The flexible cable of the MEA and the self-designed 3D printed electrode holder provided us enough space to perform two-photon imaging after the insertion, near the shanks of the MEA. The shadow of the MEA in the field of view of the two-photon objective is at the top crosswise. Neurons are observable near the shank of the MEA.

The artefacts caused by the imaging laser could have different kind of natures because of the differences in the technological parameters of the applied MEAs such as the thickness of the substrate silicon or the thickness and the material of the applied conductive layer. Having applied the self-developed custom-set comb filter based filtering and analyzing algorithm on the electrophysiological recordings it was proved to be suitable for noise elimination and spike detection on this different kind of MEA too. After eliminating the majority of the laser generated artefacts, the algorithm detected and sorted SUAs from the simultaneous *in vivo* measurements. One of the sorted SUA, its waveforms with their average and the correlated autocorrelogram is presented in Figure 4.15.

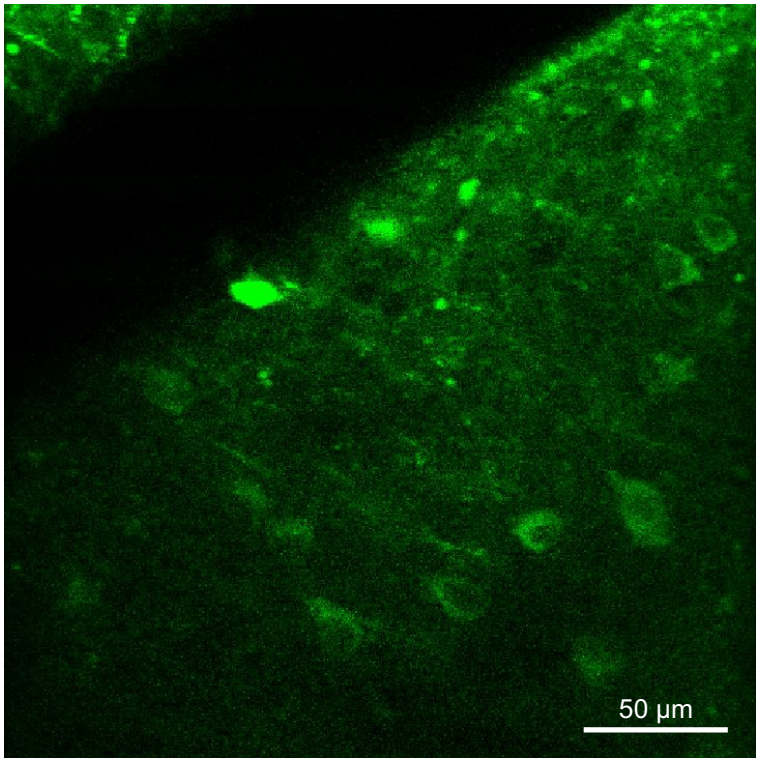

Figure 4.14: *Two-photon image from the simultaneous* in vivo *electrophysiological recording and two-photon imaging. The shadow of the MEA in the field of view of the two-photon objective is at the top crosswise. Neurons are observable near the shank of the MEA*

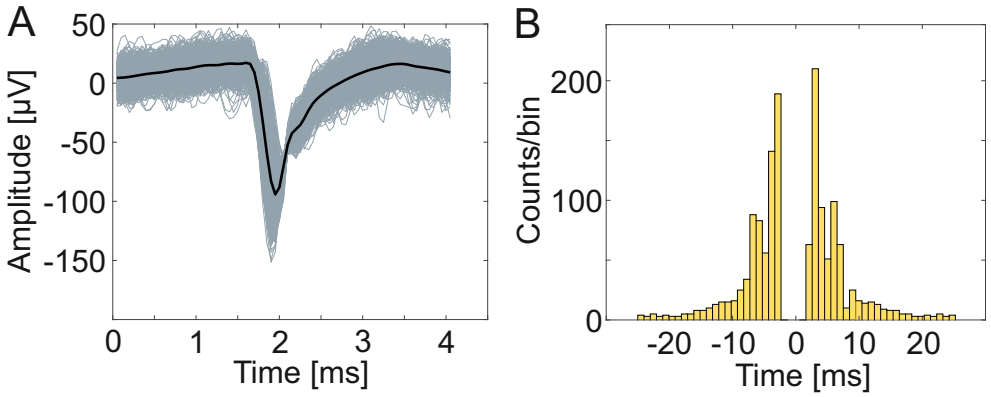

Figure 4.15: *One of the sorted SUA from* in vivo *recordings, the spike waveforms (A) with their average (black line) and the autocorrelogram of the thus sorted spike (B)*

4.2 Discussion concerning the simultaneous electrophysiological recording and two-photon imaging

Neuroscientists claim that simultaneous application of two-photon imaging and implanted MEAs would be beneficial for obtaining more complex information about the activity, connectivity and function of brain cells [67, 85, 145]. One of the major challenges of the simultaneous utilization of these state of the art methods comes from the photoelectric artifacts on the electrophysiological recordings caused by the imaging laser. This challenge was partly overcome previously with various data filtering algorithms [146]. The herein presented complex filtering method relieves this obstacle further by offering means for researchers to detect and sort SUAs from recordings affected by the laser noise of a two-photon microscope. However, the methods have still limitations. A "clean", laser noise free recording is suggested to be recorded before and after the actual simultaneous recording in order to verify the validity of the obtained spike features. Furthermore, the applied comb filter based algorithm distorts spike waveforms more than the more commonly utilized band-pass filters (with cutoff frequencies at e.g. 300 Hz and 3000 Hz). A promising alternative possibility to monitor simultaneously the extracellular activities and the morphology near the observed neurons is the utilization of the genetically encoded voltage indicators (GEVIs) [147]. GEVIs can reveal non-spiking electrical activity and resolve spike timing with sub-millisecond resolution, tasks that cannot be performed by fluorescent genetically encoded calcium indicators, but the application of the GEVIs is still challenging and it has pitfalls [148]. Since the response kinetics of a voltage indicator must be able to resolve changes on the sub-millisecond time scale, GEVIs can not be observed with traditional two-photon microscopy. Thus the utilization of a new kind of scanning method with higher frame rate is also required [149].

The presented method can be further developed by the application of an automated algorithm which determines the range of the comb filter in the frequency band, and by a more complex software which takes into account the periodicity of the laser noise for spike detection. Some efforts were made for automating the process, i.e. to solve the parameter setting step automatically, but for a sufficiently robust algorithm more work needs to be done on this matter.

4.3 Results concerning the determination of the thickness dependent electrical impedance spectrum of human dentin

The comparison of the combined absolute impedance of the working electrode and the saline to the absolute impedance of a 1 *mm* thick dentin layer according to the measuring frequency is shown in Figure 4.16. The working electrode in the chosen geometry in the silicone rubber was suitable for measuring on small examined area and it had lower impedance than the observed dentin layer, thus the applied working electrode was suitable for the dental experiments. The comparison of the phase of the combined impedance of the working electrode and the saline compared to the phase of the impedance of a 1 *mm* thick dentin layer is shown in Figure 4.17. The Bode curves indicate the capacitive nature of the observed dentin layer and the measurement system too.

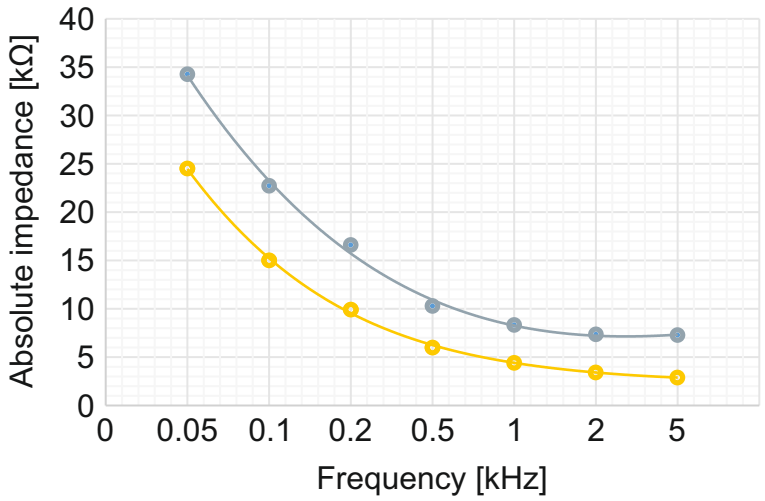

Figure 4.16: *The combined absolute impedance of the working electrode and the saline (orange) compared to the absolute impedance of a* 1 *mm thick dentin layer (gray)*

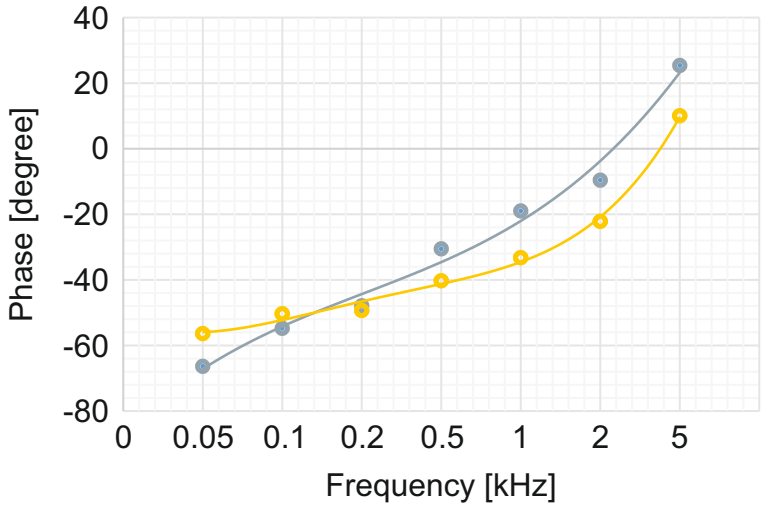

Figure 4.17: *The phase of the combined impedance of the working electrode and the saline (orange) compared to the phase of the impedance of a 1 mm thick dentin layer (gray)*

The average impedance and the standard error of the mean of each thickness group is presented at different frequencies in Figure 4.18. In order to represent the connection between the absolute impedance and the thickness of the examined dentin, the thickness-impedance coefficient of human dentin was defined as:

$$\frac{|Z|}{d}A = 8.356\ \Omega m$$

with the standard error of 0.605 Ωm at 1 kHz, where Z is the absolute impedance, d is the thickness and A is the measured area of the dentin. The thickness-impedance coefficient depends on measuring frequency. The thickness-impedance coefficient and the standard error of the mean of each observed frequency is shown in Table 4.1.

The applied statistic method proved that there are significant differences on $p = 0.002$ significance level at every observed frequency between the impedance values of each thickness group.

Frequency [kHz]	**Thickness-impedance coefficient** [Ωm]	**Standard error** [Ωm]
0.1	11.931	0.763
0.2	9.816	0.614
0.5	8.624	0.583
1	8.356	0.605
2	7.913	0.582
5	7.997	0.596

Table 4.1: *The thickness-impedance coefficient and the standard error of the mean of each observed frequency*

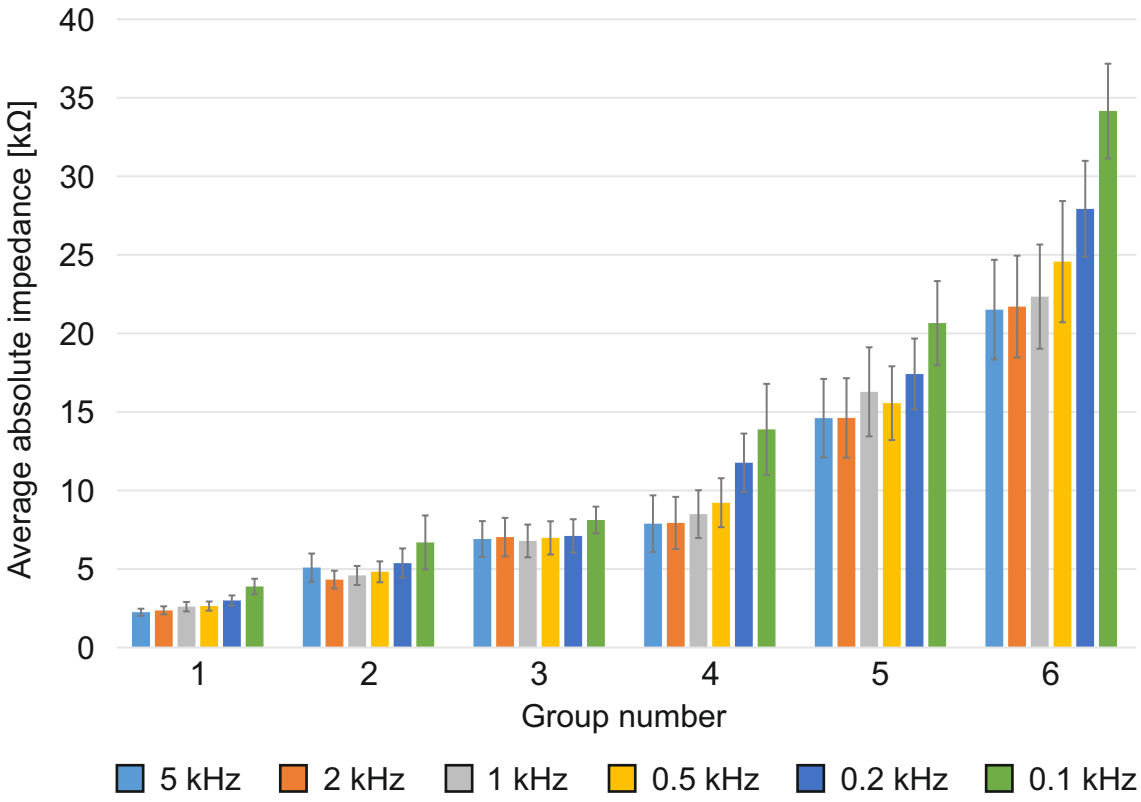

Figure 4.18: *Average impedances and their standard errors of each thickness group at different frequencies. The group numbers indicate the following thickness intervals: Group no.1: 0.30-0.44 mm, group no.2: 0.45-0.59 mm, group no.3: 0.60-0.74 mm, group no.4: 0.75-0.94 mm, group no.5: 0.95-1.24 mm, group no.6: 1.25-2.28 mm*

4.4 Discussion concerning the determination of the thickness dependent electrical impedance spectrum of human dentin

Previous studies reported the impedance of the human dentin at one specified thickness (d) and usually from a larger measurement area (A). Using the analogy of conductive materials, the measurement area can be taken into account as the cross-section and the length of a conductive material, which is inversely proportional to the impedance. Therefore, it is important to include measurement areas in the analysis if we intend to compare the values obtained by previous and future studies. With this taken into account, the thickness-impedance coefficient presented here has proven to be in the same order of magnitude as earlier studies suggested [115, 124, 150]. However, the measurements of those studies were limited to one specific thickness value. In case of measuring the impedance of the dentin perpendicularly to dental tubules, the measured impedances would be in a higher range of magnitude [151].

We used surgically removed impacted wisdom teeth in order to get similar samples where dentinal tubules were open on their entire length, also to reduce the influence of age related factors. A former study presented the age related changes in impedance spectroscopy of human dentin [120]. In terms of the age related occlusion of dental tubules, wisdom teeth are slightly comparable with the youngest focus group presented in that study. Comparing the results, if the tested thickness and the measured area are considered, the thickness-impedance coefficient provides corresponding impedance value as it was published earlier. A recent in vivo study observed the effect of cavity depth on dentin sensitivity [111]. The authors deepened the cavities and measured the electrical resistance of them to observe the distance between the bottom of the cavities and the enamel-dentin junction. Since the remaining dentin thickness was not observed, the electrical resistance values presented in that study are hardly comparable with our results.

Chapter 5

Overview of the new scientific results

5.1 First thesis group: Simultaneous utilization of electrophysiological recording and two-photon imaging

5.1.1 I.a thesis

I developed a complex custom-set comb filter based filtering algorithm which was used for data analysis to eliminate the imaging laser generated artefacts from simultaneous two-photon imaging and electrophysiological measurements. *In vitro* experiments were performed on mouse neocortical slices expressing the GCaMP6 genetically encoded calcium indicator for monitoring the neural activity with two-photon microscopy around an implanted MEA and electrophysiological recordings were made from the tissue region of the optical imaging. I proved that the applied filtering is capable of eliminating the majority of the periodic photoelectric artefacts generated by the imaging laser and this method allows single unit activity detection and sorting. Publication related to the thesis point: [R1]

5.1.2 I.b thesis

To verify the suitability of it, I have utilized the self-developed filtering algorithm on extracellular recordings from a special, MEMS technology based MEA which was developed so as to perform simultaneous electrophysiological recording and two-photon imaging from the same tissue region of mice brains expressing GCaMP6 genetically encoded calcium indicator. I proved that the filtering algorithm was

suitable for SUA detection and sorting from recordings of the self-developed MEA loaded by imaging laser generated artefacts. Publication related to the thesis point: [R1]

5.2 Second thesis: Thickness-impedance coefficient of the human dentin

I observed the impedance spectrum of dentin disks prepared from human wisdom teeth in the thickness range of $0.3 - 2.3\ mm$ to reveal the correlation between the thickness and the electrical impedance of human dentin. In accordance with the results of the performed *in vitro* experiments I determined the thickness-impedance coefficient of human dentin which is

$$\frac{|Z|}{d}A = 8.356\ \Omega m$$

with the standard error of 0.605 Ωm at 1 kHz, where Z is the absolute impedance, d is the thickness and A is the measured area of the human dentin. The thickness-impedance coefficient depends on measuring frequency. The applied statistic method proved that there are significant differences at every observed frequency between the impedance values of each thickness group. Publication related to the thesis point: [R2]

Chapter 6

Author's publication list

6.1 Papers closely related to the PhD dissertation

[R1] G. Orbán, D. Meszéna, K. R. Tasnády, B. Rózsa, I. Ulbert, G. Márton (2019): Method for spike detection from microelectrode array recordings contaminated by artifacts of simultaneous two-photon imaging, PLOS ONE 14: (8) p. e0221510.

[R2] G. Orbán, Cs. Dobó-Nagy, I. Ulbert, G. Márton (2020): Thickness dependent electrical impedance spectrum of human dentin, INTERNATIONAL JOURNAL OF CLINICAL DENTISTRY 13: (1) p105-115. 11p.

6.2 Papers not closely related to the PhD dissertation

[N1] T. Marek, G. Orbán, D. Meszéna, G. Márton, I. Ulbert, G. Mészáros, Z. Keresztes (2021): Optimization aspects of electrodeposition of photoluminescent conductive polymer layer onto neural microelectrode arrays, MATERIALS CHEMISTRY AND PHYSICS: (260) 124163

[N2] G. Márton, E. Zs. Tóth, L. Wittner, R. Fiáth, D. Pinke, G. Orbán, D. Meszéna, I. Pál, E. L. Győri, Zs. Bereczki, Á. Kandrács, K. T. Hofer, A. Pongrácz, I. Ulbert, K. Tóth (2020): The neural tissue around SU-8 implants: A quantitative in vivo biocompatibility study, MATERIALS SCIENCE AND ENGINEERING: C 112: 110870

[N3] A. Zátonyi, G. Orbán, R. Modi, G. Márton, D. Meszéna, I. Ulbert, A. Pongrácz, M. Ecker, E. W. Voit, A. Joshi-Imre, Z. Fekete (2019): A softening laminar electrode for recording single unit activity from the rat hippocampus, SCIENTIFIC REPORTS 9: (1) 2321

[N4] D. Meszéna, P. B. Kerekes, I. Pál, G. Orbán, R. Fiáth, T. Holzhammer, P. Ruther, I. Ulbert, G. Márton (2019): A silicon-based spiky probe providing improved cell accessibility during in vitro slice recordings, SENSORS AND ACTUATORS B-CHEMICAL 297: 126649

[N5] G. Márton, M. Kiss, G. Orbán, A. Pongrácz, I. Ulbert (2015): A polymer-based spiky microelectrode array for electrocorticography, MICROSYSTEM TECHNOLOGIES 21: (3) pp. 619-624.

[N6] G. Márton, G. Orbán, Kiss Marcell, R. Fiáth, A. Pongrácz, I. Ulbert (2015): A Multimodal, SU-8-Platinum - Polyimide Microelectrode Array for Chronic In Vivo Neurophysiology, PLOS ONE 10: (12) e0145307

[N7] G. Márton, G. Orbán, M. Kiss, A. Pongrácz, I. Ulbert (2014): A Novel Polyimide – Platinum – SU-8 Microelectrode Array for Various Electrophysiological Applications, PROCEDIA ENGINEERING 87: pp. 380-383.

[N8] G. Márton, G. Orbán, R. Fiáth, I. Bakos, Z. Fekete, A. Pongrácz, I. Ulbert (2014): MEMS érzékelők a neurofiziológiában, MTA Természettudományi Kutatóközpont Doktori Konferencia, (2014) pp. 56-57.

6.3 Utility patents

[P1] I. Ulbert, G. Márton, D. Pinke, B. P. Kerekes, G. Orbán, K. R. Tasnády, D. Meszéna (2017): Multielectrode equipment with ion-conduction channel and application procedure to eliminate photoelectric noise, submitted to the Hungarian Intellectual Property Office, Application number: P1700527

[P2] G. Márton, G. Orbán, I. Ulbert (2015): Carrier device for implanting a flexible implant into a biological tissue, granted by the Hungarian Intellectual Property Office, Application number: P1500592

[P3] Cs. Dobó Nagy, G. Orbán, G. Márton (2019): Equipment for measuring the thickness of the human dentin, submitted to the Hungarian Intellectual Property Office, Application number: U1900110

Chapter 7

Acknowledgements

At the end of my doctoral studies I would like to say thank some colleagues of mine without whom the scientific work presented in this dissertation could not have been fulfilled.

I owe special thanks to Gergely Márton for his support and his guidance he gave me in the last seven and a half years. I am grateful to had you as a supervisor and as a leader of my research projects. You were not the supervisor I deserved but the one I needed.

I would like to thank to Csaba Dobó Nagy for his persistent guidance in the dental project at the Semmelweis University. Thank you for being so patient at the beginning with the incompetent engineer in a medical research. I really hope that our cooperation will be useful for the clinical dentistry someday in the near future.

I am thankful to Domokos Meszéna for his tireless support during the two-photon measurements and for the precise work he performed in the brain slice preparation for the simultaneous *in vitro* recordings.

I owe Judit Borsa a debt of gratitude for her quick and accurate help in terms of the administrative guidance of my doctoral studies.

The project of the first and the second thesis points was supported by the ÚNKP-18-3-I-OE-105 New National Excellence Program of the Ministry of Human Capacities and by the ÚNKP-19-3-I-OE-60 New National Excellence Program of the Ministry for Innovation and Technology.

List of Figures

Bibliography

[1] A.L. Hodgkin and A.F. Huxley. A quantitative description of membrane current and its application to conduction and excitation in nerve. *The Journal of Physiology*, 117(4):500–544, 1952. PMCID: PMC1392413.

[2] T. Goto, R. Hatanaka, T. Ogawa, A. Sumiyoshi, J. Riera, and R. Kawashima. An evaluation of the conductivity profile in the somatosensory barrel cortex of wistar rats. *Journal of Neurophysiology*, 104(6):3388–412, 2010. Using Smart Source Parsing Dec; doi: 10.1152/jn.00122.2010. Epub 2010 Sep 1.

[3] C. Nicholson and J.A. Freeman. Theory of current source-density analysis and determination of conductivity tensor for anuran cerebellum. *Journal of Neurophysiology*, 38(2):356–68, 1975. Using Smart Source Parsing Mar.

[4] N. Teplan. Fundamentals of eeg measurement. *Measurement Science review*, 2(2):2002, 2002.

[5] H. Gelbard-Sagiv, R. Mukamel, M. Harel, R. Malach, and I. Fried. Internally generated reactivation of single neurons in human hippocampus during free recall. *Science*, 322(5898):96–101, 2008. Using Smart Source Parsing Oct 3; doi: 10.1126/science.1164685. Epub 2008 Sep 4.

[6] H. Liu, N. Tanaka, S. Stufflebeam, S. Ahlfors, and M. Hamalainen. Functional mapping with simultaneous meg and eeg. *Journal of Visualized Experiments*, 14(40):1668, 2010.

[7] L.M. Oberman, E.M. Hubbard, J.P. McCleery, E.L. Altschuler, V.S. Ramachandran, and J.A. Pineda. Eeg evidence for mirror neuron dysfunction in autism spectrum disorders. *Brain Research, Cognitive Brain Research*, 24(2):190–8, 2005. Using Smart Source Parsing Jul.

[8] S.J. Smith. Eeg in the diagnosis, classification, and management of patients with epilepsy. *Journal of Neurology, Neurosurgery, and Psychiatry*, 76(2):ii2–7, 2005. Using Smart Source Parsing Jun;Suppl.

[9] J.S. Perlmutter and J.W. Mink. Deep brain stimulation. *Annual Review of Neuroscience*, 29:229–257, 2006. PMID: 16776585.

[10] B.J. Edelman, B. Baxter, and B. He. No TitleEEG Source Imaging Enhances the Decoding of Complex Right-Hand Motor Imagery Tasks. *IEEE Transactions on Biomedical Engineering*, 63(1):4–14, 2016.

[11] Leigh R. Hochberg, Daniel Bacher, Beata Jarosiewicz, Nicolas Y. Masse, John D. Simeral, Joern Vogel, Sami Haddadin, Jie Liu, Sydney S. Cash, Patrick Van der Smagt, and John P. Donoghue. Reach and grasp by people with tetraplegia using a neurally controlled robotic arm. *Nature*, 485:372–375, 2012.

[12] G. Hotson, D.P. McMullen, M.S. Fifer, M.S. Johannes, K.D. Katyal, M.P. Para, R. Armiger, W.S. Anderson, N.V. Thakor, B.A. Wester, and N.E. Crone. Individual finger control of a modular prosthetic limb using high-density electrocorticography in a human subject. *Journal of Neural Engineering*, 13(2):26017, 2016.

[13] Douglas J. Weber Daniel W. Moran Andrew B. Schwartz, X. Tracy Cui. Brain-controlled interfaces: Movement restoration with neural prosthetics. *Neuron*, 2006.

[14] Fernando Lopes da Silva Ernst Niedermeyer. *Electroencephalography : basic principles, clinical applications, and related fields.* Lippincott Williams and Wilkins, 2005.

[15] B Keri, Sz.; Gulyas. *Elektrofiziológiai módszerek a kognitív idegtudományban.* Osiris Kiadó, 2003.

[16] Tracey; Muscat Joseph; Camilleri Kenneth P.; Fabri Simon G.; Zervakis Michalis; Xanthopoulos Petros; Sakkalis Vangelis; Vanrumste Bart Grech, Roberta; Cassar. Review on solving the inverse problem in eeg source analysis. *Journal of NeuroEngineering and Rehabilitation*, 5(25):1743–0003, 2008. PMID: 18990257.

[17] Wolfgang Klimesch. Eeg alpha and theta oscillations reflect cognitive and memory performance: a review and analysis. *Brain Research Reviews*, 29(2â€“3):169–195, 1999.

[18] Sheng-Fu Liang, Hsu-Chuan Wang, and Wan-Lin Chang. Combination of eeg complexity and spectral analysis for epilepsy diagnosis and seizure detection. *EURASIP Journal on Advances in Signal Processing*, 2010:62, 2010.

[19] M.B. Sterman. Basic concepts and clinical findings in the treatment of seizure disorders with eeg operant conditioning. *Clinical Electroencephalography*, 31(1):45–55, 2000. Using Smart Source Parsing Jan.

[20] Jonathan R. Wolpaw, Niels Birbaumer, Dennis J. McFarland, Gert Pfurtscheller, and Theresa M. Vaughan. Brain-computer interfaces for communication and control. *Clinical Neurophysiology*, 113(6):767 – 791, 2002.

[21] C. Neuper, G. R. MĂĽller, A. KĂĽbler, N. Birbaumer, and G. Pfurtscheller. Clinical application of an eeg-based brain computer interface: a case study in a patient with severe motor impairment. *Clinical Neurophysiology*, 114(3):399–409, 2003.

[22] Conrado; Oostenveld Robert; Fries Pascal; Stieglitz Thomas Rubehn, Birthe; Bosman. A mems-based flexible multichannel ecog-electrode array. *Journal of Neural Engineering*, 6(3):036003, 2009.

[23] A.K. Engel, C.K. Moll, I. Fried, and G.A. Ojemann. Invasive recordings from the human brain: clinical insights and beyond. *Nature Reviews Neuroscience*, 6(1):35–47, 2005. Using Smart Source Parsing Jan.

[24] M.S. Jones and D.S. Barth. Spatiotemporal organization of fast (>200 hz) electrical oscillations in rat vibrissa/barrel cortex. *Journal of Neurophysiology*, 82(3):1599–609, 1999. Using Smart Source Parsing Sep.

[25] H. Sugano, H. Shimizu, and S. Sunaga. Efficacy of intraoperative electrocorticography for assessing seizure outcomes in intractable epilepsy patients with temporal-lobe-mass lesions. *Seizure*, 16(2):120–7, 2007. Using Smart Source Parsing Mar; Epub 2006 Dec 8.

[26] R. Scherer, S.P. Zanos, K.J. Miller, R.P. Rao, and J.G. Ojemann. Classification of contralateral and ipsilateral finger movements for electrocorticographic brain-computer interfaces. *Neurosurgical Focus*, 27(1):E12, 2009.

[27] V.G. Kanas, I. Mporas, H.L. Benz, K.N. Sgarbas, A. Bezerianos, and N.E. Crone. Joint spatial-spectral feature space clustering for speech activity detection from ecog signals. *IEEE Transactions on Biomedical Engineering*, 61(4):1241–50, 2014. Using Smart Source Parsing Apr; doi: 10.1109/TBME.2014.2298897.

[28] Gergely Márton, Gábor Orbán, Marcell Kiss, Richárd Fiáth, Anita Pongrácz, and István Ulbert. A Multimodal, SU-8 - Platinum - Polyimide Microelectrode Array for Chronic In Vivo Neurophysiology. *PLoS ONE*, 10(12), 2015.

[29] Richárd Fiáth, Bogdan Cristian Raducanu, Silke Musa, Alexandru Andrei, Carolina Mora Lopez, Chris van Hoof, Patrick Ruther, Arno Aarts, Domonkos Horváth, and István Ulbert. A silicon-based neural probe with densely-packed low-impedance titanium nitride microelectrodes for ultrahigh-resolution in vivo recordings. *Biosensors and Bioelectronics*, 106:86–92, 2018.

[30] Marieke L. Schölvinck, David A. Leopold, Matthew J. Brookes, and Patrick H. Khader. The contribution of electrophysiology to functional connectivity mapping. *NeuroImage*, 80:297–306, 2013.

[31] Shinya Ito, Fang-Chin Yeh, Emma Hiolski, Przemyslaw Rydygier, Deborah E. Gunning, Pawel Hottowy, Nicholas Timme, Alan M. Litke, and John M. Beggs. Large-Scale, High-Resolution Multielectrode-Array Recording Depicts Functional Network Differences of Cortical and Hippocampal Cultures. *PLoS ONE*, 9(8), 2014.

[32] Peter Konrad and Todd Shanks. Implantable brain computer interface: Challenges to neurotechnology translation. *Neurobiology of Disease*, 38(3):369–375, 2010.

[33] S.P. Kim, J.D. Simeral, L.R. Hochberg, J.P. Donoghue, G. M. Friehs, and M.J. Black. Point-and-click cursor control with an intracortical neural interface system by humans with tetraplegia. *IEEE Transactions on Neural Systems and Rehabilitation Engineering*, 19(2):193–203, 2011.

[34] Francis Willett, Brian Murphy, William Memberg, Christine Blabe, Chethan Pandarinath, Benjamin Walter, Jennifer Sweet, Jonathan Miller, Jaimie Henderson, Krishna Shenoy, Leigh Hochberg, Robert Kirsch, and A. Ajiboye. Signal-independent noise in intracortical brain–computer interfaces causes movement time properties inconsistent with fitts' law. *Journal of Neural Engineering*, 14:026010, 04 2017.

[35] Chethan Pandarinath, Paul Nuyujukian, Christine Blabe, Brittany Sorice, Jad Saab, Francis Willett, Leigh Hochberg, Krishna Shenoy, and Jaimie Henderson. High performance communication by people with paralysis using an intracortical brain-computer interface. *eLife*, 6, 02 2017.

[36] Paul Nuyujukian, Jose Albites Sanabria, Jad Saab, Chethan Pandarinath, Beata Jarosiewicz, Christine H. Blabe, Brian Franco, Stephen T. Mernoff, Emad N. Eskandar, John D. Simeral, Leigh R. Hochberg, Krishna V. Shenoy, and Jaimie M. Henderson. Cortical control of a tablet computer by people with paralysis. *PLoS ONE*, 13(11):1–16, 11 2018.

[37] Meel Velliste, Sagi Perel, Chance Spalding, Andrew Whitford, and Andrew Schwartz. Cortical control of a prosthetic arm for self-feeding. *Nature*, 453:1098–101, 05 2008.

[38] Peter Ifft, Solaiman Shokur, Zheng Li, Mikhail Lebedev, and Miguel Nicolelis. A brain-machine interface enables bimanual arm movements in monkeys. *Science translational medicine*, 5:210ra154, 11 2013.

[39] William Bishop, Cynthia Chestek, Vikash Gilja, Paul Nuyujukian, Justin Foster, Stephen Ryu, Krishna Shenoy, and Byron Yu. Self-recalibrating classifiers for intracortical brain-computer interfaces. *Journal of neural engineering*, 11:026001, 02 2014.

[40] Paul Nuyujukian, Jonathan Kao, Joline Fan, Sergey Stavisky, Stephen Ryu, and Krishna Shenoy. Performance sustaining intracortical neural prostheses. *Journal of Neural Engineering*, 11:066003, 10 2014.

[41] Leigh Hochberg, Mijail Serruya, Gerhard Friehs, Jon Mukand, Maryam Saleh, Abraham Caplan, Almut Branner, David Chen, Richard Penn, and John Donoghue. Neuronal ensemble control of prosthetic devices by a human with tetraplegia. *Nature*, 442:164–71, 08 2006.

[42] Brian Wodlinger, John Downey, Elizabeth Tyler-Kabara, Andrew Schwartz, M. Boninger, and Jennifer Collinger. Ten-dimensional anthropomorphic arm control in a human brain-machine interface: Difficulties, solutions, and limitations. *Journal of neural engineering*, 12:016011, 12 2014.

[43] Jennifer L. Collinger, Brian Wodlinger, John E. Downey, Wei Wang, Elizabeth C. Tyler-Kabara, Douglas J. Weber, Angus J.C. McMorland, Meel Velliste, Michael L. Boninger, and Andrew B. Schwartz. High-performance neuroprosthetic control by an individual with tetraplegia. *Lancet*, 381:557–564, 2013.

[44] Arto Nurmikko, John Donoghue, Leigh Hochberg, William Patterson, Yoon-Kyu Song, Christopher Bull, David Borton, Farah Laiwalla, Sunmee Park, Ming Yin, and Juan Aceros. Listening to brain microcircuits for interfacing with external world-progress in wireless implantable microelectronic neuroengineering devices: Experimental systems are described for electrical recording in the brain using multiple microelectrodes and short range implantable or wearable broadcasting units. *Proceedings of the IEEE. Institute of Electrical and Electronics Engineers*, 98:375–388, 03 2010.

[45] Joana P. Neto, Gonçalo Lopes, João Frazão, Joana Nogueira, Pedro Lacerda, Pedro Baião, Arno Aarts, Alexandru Andrei, Silke Musa, Elvira Fortunato, Pedro Barquinha, and Adam R. Kampff. Validating silicon polytrodes with paired juxtacellular recordings: method and dataset. *Journal of Neurophysiology*, 116(2):892–903, 2016.

[46] J.C. Barrese, N. Rao, K. Paroo, C. Triebwasser, C. Vargas-Irwin, L. Franquemont, and J.P. Donoghue. Failure mode analysis of silicon-based intracortical microelectrode arrays in non-human primates. *Journal of Neural Engineering*, 10(6):66014, 2013.

[47] Patrick J. Rousche and Richard A. Normann. Chronic recording capability of the Utah Intracortical Electrode Array in cat sensory cortex. *Journal of Neuroscience Methods*, 82(1):1–15, 1998.

[48] Takashi D.Y. Kozai, Andrea S. Jaquins-Gerstl, Alberto L. Vazquez, Adrian C. Michael, and X. Tracy Cui. Brain Tissue Responses to Neural Implants Impact Signal Sensitivity and Intervention Strategies. *ACS Chemical Neuroscience*, 6(1):48–67, 2015.

[49] Takashi D.Y. Kozai, Kasey Catt, Xia Li, Zhannetta V. Gugel, Valur T. Olaffson, Alberto L. Vazquez, and Tracy X. Cui. Mechanical failure modes of chronically implanted planar silicon-based neural probes for laminar recording. *Biomaterials*, 37:25–39, 2015.

[50] P.J. Gilgunn, Xiao Chuan O., S.N. Flesher, A.B. Schwartz, and R.A. Gaunt. Structural analysis of explanted microelectrode arrays. In *Neural Engineering (NER), 2013 6th International IEEE/EMBS Conference*, pages 719–722, 2013.

[51] L. Karumbaiah, S.E. Norman, N.B. Rajan, S. Anand, T. Saxena, M. Betancur, R. Patkar, and R.V. Bellamkonda. The upregulation of specific interleukin (IL) receptor antagonists and paradoxical enhancement of neuronal apoptosis due to electrode induced strain and brain micromotion. *Biomaterials*, 33(26):5983–5996, 2012.

[52] Vadim S. Polikov, Patrick A. Tresco, and William M. Reichert. Response of brain tissue to chronically implanted neural electrodes. *Journal of Neuroscience Methods*, 148(1):1–18, 2005.

[53] A. Prasad, Q.S. Xue, V. Sankar, T. Nishida, G. Shaw, W.J. Streit, and J.C. Sanchez. Comprehensive characterization and failure modes of tungsten microwire arrays in chronic neural implants. *Journal of Neural Engineering*, 9(5):56015, 2012.

[54] Elizabeth M.C. Hillman. Optical brain imaging in vivo: techniques and applications from animal to man. *Journal of Biomedical Optics*, 12(5):51402, 2007.

[55] André Fiala, Anna Suska, and Oliver M. Schlüter. Optogenetic Approaches in Neuroscience. *Current Biology*, 20(20):R897–R903, 2010.

[56] Peter T.C. So, Chen Y. Dong, Barry R. Masters, and Keith M. Berland. Two-photon excitation fluorescence microscopy. *Annual Review of Biomedical Engineering*, 2:399–429, 2000.

[57] Martín A. Bertrán, Natalia L. Martínez, Ye Wang, David Dunson, Guillermo Sapiro, and Dario Ringach. Active learning of cortical connectivity from two-photon imaging data. *PLoS ONE*, 13(5), 2018.

[58] Cher Bass, Pyry Helkkula, Vincenzo De Paola, Claudia Clopath, and Anil Anthony Bharath. Detection of axonal synapses in 3D two-photon images. *PLoS ONE*, 12(9), 2017.

[59] Jason N.D. Kerr, David S. Greenberg, and Fritjof Helmchen. Imaging input and output of neocortical networks in vivo. *Proceedings of the National Academy of Sciences of the United States of America*, 102(39):14063–14068, 2005.

[60] Jason N.D. Kerr, Christiaan P.J. de Kock, David S. Greenberg, Randy M. Bruno, Bert Sakmann, and Fritjof Helmchen. Spatial Organization of Neuronal Population Responses in Layer 2/3 of Rat Barrel Cortex. *The Journal of Neuroscience*, 27(48):13316–13328, 2007.

[61] C. Stosiek, O. Garaschuk, K. Holthoff, and A. Konnerth. In vivo two-photon calcium imaging of neuronal networks. *Proceedings of the National Academy of Sciences of the United States of America*, 100(12):7319–7324, 2003.

[62] Wasim Q. Malik, James Schummers, Mriganka Sur, and Emery N. Brown. Denoising Two-Photon Calcium Imaging Data. *PLoS ONE*, 6(6), 2011.

[63] Winfried Denk; James H Strickler; Watt W Webb. Two-photon laser scanning fluorescence microscopy. *Science*, 248(4951):73–76, 1990.

[64] Karel Svoboda; Ryohei Yasuda. Principles of two-photon excitation microscopy and its applications to neuroscience. 50(6):823–839, 2006.

[65] Shaun Pacheco, Chengliang Wang, Monica K. Chawla, Minhkhoi Nguyen, Brend K. Baggett, Urs Utzinger, Carol A. Barnes, and Rongguang Liang.

High resolution, high speed, long working distance, large field of view confocal fluorescence microscope. *Scientific Reports*, 7(1):2045–2322, 2017.

[66] Takashi D.Y. Kozai, James R. Eles, Alberto L. Vazquez, and Tracy X. Cui. Two-photon imaging of chronically implanted neural electrodes: Sealing methods and new insights. *Journal of Neuroscience Methods*, 258:46–55, 2016.

[67] Dong-Wook Park, Sarah K. Brodnick, Jared P. Ness, Farid Atry, Lisa Krugner-Higby, Amelia Sandberg, Solomon Mikael, Thomas J. Richner, Joseph Novello, Hyungsoo Kim, Dong-Hyun Baek, Jihye Bong, Seth T. Frye, Sanitta Thongpang, Kyle I. Swanson, Wendell Lake, Ramin Pashaie, Justin C. Williams, and Zhenqiang Ma. Fabrication and utility of a transparent graphene neural electrode array for electrophysiology, in vivo imaging, and optogenetics. *Nature Protocols*, 11:2201–2222, 2016.

[68] Patrick J. Rousche, David S. Pellinen, David P. Pivin, Justin C. Williams, Rio J. Vetter, and Daryl R. Kipke. Flexible polyimide-based intracortical electrode arrays with bioactive capability. *IEEE Transactions on Biomedical Engineering*, 48(3):361–371, 2001.

[69] Der-Jang Liaw, Kung-Li Wang, Ying-Chi Huang, Kueir-Rarn Lee, Juin-Yih Lai, and Chang-Sik Ha. Advanced polyimide materials: Syntheses, physical properties and applications. *Progress in Polymer Science*, 37(7):907 – 974, 2012. Topical Issue on Polymer Synthesis.

[70] Hong jiang Ni, Jin gang Liu, Zhen he Wang, and Shi yong Yang. A review on colorless and optically transparent polyimide films: Chemistry, process and engineering applications. *Journal of Industrial and Engineering Chemistry*, 2015.

[71] Jingquan Liu, B. Cai, Jacob Zhu, Guifu Ding, X. Zhao, C. Yang, and Di Chen. Process research of high aspect ratio microstructure using su-8 resist. *Microsystem Technologies*, 10:265–268, 05 2004.

[72] Wanjun Wang Ren Yang, Steve Allan Soper. Microfabrication of an integrated su-8 waveguide with an embedded focusing lens for application in single-molecule detection (smd). *Materials Science, Engineering*, 2005.

[73] John M. Nagarah; AnnetteStowasser; RellL.Parker; HirokiAsari; Daniel A.Wagenaar. Optically transparent multi-suction electrode arrays. *Frontiers in Neuroscience*, 2015.

[74] Gagan Kaur; Raju Adhikari; Peter Cass; Mark Bown; Pathiraja Gunatillake. Electrically conductive polymers and composites for biomedical applications. *RSC Advances*, 5(37553), 2015.

[75] Rajeswari Ravichandran; Subramanian Sundarrajan; Jayarama Reddy Venugopal; Shayanti Mukherjee; Seeram Ramakrishna. Applications of conducting polymers and their issues in biomedical engineering. *Journal of the Royal Society Interface*, 7:S559–S579, 2010.

[76] Mohammad Reza Abidian; David C. Martin. Experimental and theoretical characterization of implantable neural microelectrodes modified with conducting polymer nanotubes. *Biomaterials*, 29:1273–1283, 2008.

[77] Martin Xinyan Cuia; James Wilerb; Marta Dzamanb; Richard A, Altschulerb; David C. In vivo studies of polypyrrole/peptide coated neural probes. *Biomaterials*, 24:77–787, 2003.

[78] Kip A. Ludwig; Jeffrey D. Uram; Junyan Yang; David C. Martin; Daryl R. Kipke. Chronic neural recordings using silicon microelectrode arrays electrochemically deposited with a poly(3,4-ethylenedioxythiophene) (pedot) film. *Journal of Neural Engineering*, 3:59–70, 2006.

[79] Xinyan Cuia; David C. Martin. Electrochemical deposition and characterization of poly(3,4-ethylenedioxythiophene) on neural microelectrode analysis. *Sensors and Actuators*, 89:92–102, 2003.

[80] Rylie A. Green; Nigel H. Lovell; Gordon G. Wallace; Laura A Poole-Warren. Conducting polymers for neural interfaces: Challenges in developing an effective long-term implant. *Biomaterials*, 29:3393–3399, 2008.

[81] Amelia A. Schendel; Kevin W. Eliceiri; Justin C. Williams. Advanced materials for neural surface electrodes. *Current Opinion in Solid State and Materials Science*, 18(6):301–307, 2014.

[82] Bertalan K. Andrasfalvy; Gregorio L. Galinanes; Daniel Huber; Mladen Barbic; John J. Macklin; Kimihiro Susumu; James B. Delehanty; Alan L. Huston; Judit K. Makara; Igor L. Medintz. Quantum dot–based multiphoton fluorescent pipettes for targeted neuronal electrophysiology. *Nature Methods*, 2014.

[83] Kenath Priyanka Prasad; Yun Chen; Mahasin Alam Sk; Aung Than; Yue Wang; Handong Sun; Kok-Hwa Lim; Xiaochen Dongc; Peng Chen. Fluorescent quantum dots derived from pedot and their applications in optical imaging and sensing. *Materials Horizons*, 1:529–534, 2014.

[84] D. Kuzum, H. Takano, E. Shim, J.C. Reed, H. Juul, A.G. Richardson, J. de Vries, H. Bink, M.A. Dichter, T.H. Lucas, D.A. Coulter, E. Cubukcu, and B. Litt. Transparent and flexible low noise graphene electrodes for simultaneous electrophysiology and neuroimaging. *Nature Communications*, 20(5):5259, 2014.

[85] Takashi D.Y. Kozai and Alberto L. Vazquez. Photoelectric artefact from optogenetics and imaging on microelectrodes and bioelectronics: new challenges and opportunities. *Journal of Materials Chemistry B*, 3(25):4935–5124, 2015.

[86] Tongsheng Zhang and Yoshio Okada. Recursive artifact windowed–single tone extraction method (RAW–STEM) as periodic noise filter for electrophysiological signals with interfering transients. *Journal of Neuroscience Methods*, 155:308–318, 2006.

[87] H. Prance, R.J. Prance, and P.B. Stiffell. Hardware comb filter enhances dynamic range and noise performance of sensors in noisy environments. *Review of Scientific Instruments*, 78(074701), 2007.

[88] A. Materka and M. Byczuk. Using comb filter to enhance SSVEP for BCI applications. In *3rd Int. Conf. MEDSIP 2006, Advances in Medical, Signal and Information Processing, Glasgow*, 2006.

[89] Anna Chabuda, Piotr Durka, and Jarosław Zygierewicz. High frequency ssvep-bci with hardware stimuli control and phase- synchronized comb filter. *IEEE Transactions on Neural Systems and Rehabilitation Engineering*, 26(2), 2018.

[90] Vincent Wu, Israel M. Barbash, Kanishka Ratnayaka, Christina E. Saikus, Merdim Sonmez, Ozgur Kocaturk, Robert J. Lederman, and Anthony Z. Faranesh. Adaptive Noise Cancellation to Suppress Electrocardiography Artifacts During Real-Time Interventional MRI. *Journal of Magnetic Resonance Imaging*, 33:1184–1193, 2011.

[91] Serdar Kockanat and Serkan Kockanat. Analysis and Extraction of Fetal Electrocardiogram Signal with Adaptive Filtering Using Differential Evolution Algorithm. *Cumhuriyet Science Journal*, 39(1):294–302, 2018.

[92] Grayson W. Marshall Jr, Sally J. Marshall, John H. Kinney, and Mehdi Balooch. The dentin substrate: structure and properties related to bonding. *Journal of Dentistry*, 25(6):441–458, 1997.

[93] Staffan Olsson, Gudbrand Öilo, and Ewa Adamczak. The structure of dentin surfaces exposed for bond strength measurements. *European Journal of Oral Sciences*, 101:180–184, 1993.

[94] Gisle Fosse, Paul K. Saele, and Rune Eide. Numerical density and distributional pattern of dentin tubules. *Acta Odontologica Scandinavica*, 50(4):201–210, 1992.

[95] D.H. Pashley. Dentin: A dynamic substrate - A review. *Scanning microscopy*, 3(1):161–174, 1989.

[96] R. Garberoglio and M. Brännström. Scanning electron microscopic investigation of human dental tubules. *Archives of Oral Biology*, 2:355–362, 1976.

[97] Szentágothai János; Réthelyi Miklós. *Funkcionális Anatómia*. Medicina Kiadó, 1989. ISBN 963-241-789-5.

[98] Dr. Fazekas Árpád. *Megtartó fogászat és endodoncia*. Semmelweis Kiadó, 2006. ISBN: 9789639656123.

[99] Matti Narhi, Lars Bjørndal, Maria Pigg, Inge Fristad, and Sivakami Haug. Acute dental pain i : pulpal and dentinal pain. *Den Norske tannlaegeforenings tidende*, 126:10–18, 01 2016.

[100] L. Olgart. Local mechanism in dental pain, Mechanisms of Pain and Analgesic Compounds. *Racen Press*, pages 285–294, 1979.

[101] L. Olgart. Neural control of pulpal blood flow. *Critical Reviews in Oral Biology & Medicine*, 7(2):159–171, 1996.

[102] D.J. Anderson, A.G. Hannam, and B. Mathews. Sensory mechanisms in mammalian teeth and their supporting structures. *American Physiological Society*, 50(2):171–195, 1970.

[103] D. Andrew and B. Matthews. Displacement of the contents of dentinal tubules and sensory transduction in intradental nerves of the cat. *Journal of Physiology*, 529(3):791–802, 2000.

[104] G. Karmos, Csaba Dobo-Nagy, E. Tobias, and E. Varga. Small Area Dentin Recording by a New Technique. In *IADR General Session 2010*, 2010.

[105] J.M. Mumford and A.V. Newton. Transduction of hydrostatic pressure to electric potential in human dentin. *Journal of Dental Research*, 48(2):226–229, 1969.

[106] Avinash Ramchandra Salgar, Shishir H. Singh, Rajesh S. Podar, Gaurav P. Kulkarni, and Shashank N. Babel. Determining predictability and accuracy of thermal and electrical dental pulp tests: An in vivo study. *Journal of Conservative Dentistry*, 20(1):46–49, 2017.

[107] Eugene Chen and Paul Abbott V. Dental pulp testing: A review. *International Journal of Dentistry*, 2009, 2009.

[108] M.V.O. Närhi, T.J. Hirvonen, and M.O.K. Hakumäki. Responses of intradental nerve fibres to stimulation of dentine and pulp. *Acta Physiologica Scandinavica*, 115:173–178, 1982.

[109] H. Horiuchi and B. Matthews. Evidence on the origin of impulses recorded from dentine in the cat. *The Journal of Physiology*, 242:797–829, 1974.

[110] Cian Emilio Chatrian, Vera M Fernandes de Lima, Ettore Lettich, Robert C Canfield, R Colin Miller, and Michael J Soso. Electrical Stimulation of Tooth Pulp in Humans. II. Qualities of sensations. *Elsevier Biomedical Press*, 14:233–246, 1982.

[111] Sitthichai Wanachantararak, Orapin Ajcharanukul, Noppakun Vongsavan, and Bruce Matthews. Effect of cavity depth on dentine sensitivity in man. *Archives of Oral Biology*, 66:120–128, 2016.

[112] S.W. Cadden, S.J.W. Lisney, and B. Matthews. Thresholds to electrical stimulation of nerves in cat canine tooth-pulp with Aβ-, Aδ- and C-fibre conduction velocities. *Brain Research, Elsevier Biomedical Press*, 261:31–41, 1983.

[113] Jeremy Sword, David Pashley, Stephen Foulger, Frank Tay, and Robert Rodgers. Use of electrochemical impedance spectroscopy to evaluate resin-dentin bonds. *Journal of biomedical materials research. Part B, Applied biomaterials*, 84:468–77, 02 2008.

[114] J.H. Kinney, S.J. Marshall, and G.W. Marshall. The mechanical properties of human dentin: a critical review and re-evaluation of the dental literature. *Critical Reviews in Oral Biology & Medicine*, 14(1):13–29, 2003.

[115] J.M. Mumford. Resistivity of human enamel and dentine. *Archives of Oral Biology*, 12:925–927, 1967.

[116] D.K. Ahn, E.A. Doutova, K. McNaughton, A.R. Light, M. Närhi, and W. Maixner. Functional Properties of Tooth Pulp Neurons Responding to Thermal Stimulation. *Journal of Dental Research*, 91(4), 2012.

[117] J. Reyes-Gasga, G.R. García, O. Alvarez-Fregoso, J.A. Chávez-Carvayar, and L.E. Vargas-Ulloa. Conductivity in human tooth enamel. *Journal of materials science*, 34:2183 – 2188, 1999.

[118] A. Schulte, M. Gente, K. Pieper, and J. Arends. The electrical resistance of enamel-dentine cylinders. Influence of NaCl content in storage solutions. *Journal of Dentistry*, 26(2):113–118, 1998.

[119] Aziza Eldarrat, Alec High, and Girish Kale. Influence of sodium chloride content in electrolyte solution on electrochemical impedance measurements of human dentin. *Dental Research Journal*, 14(1):25–31, 2017.

[120] Aziza Eldarrat, Alec High, and Girish Kale. Age-related changes in ac-impedance spectroscopy studies of normal human dentine: further investigations. *Journal of Materials Science: Materials in Medicine*, 21:45–51, 2010.

[121] P. Pincus. A new method of examination of molar teeth grooves for the presence of dental caries. *The Journal of Physiology*, 113:13–14, 1951.

[122] J.M. Mumford. Relationship between the electrical resistance of human teeth and the presence and extent of dental caries. *British Dental Journal*, 100:239–244, 1965.

[123] H. Nomura, S. Sakada, and H. Itow. Some observations on electric conductivity of the tooth. *The Bulletin of Tokyo Dental College Journal*, 12:15–23, 1971.

[124] T.J. VanderNoot and M. Levinkind. AC impedance characteristics of human dental enamel and dentine. *Journal of Electroanalytical Chemistry*, 300:191–198, 1991.

[125] Ying-Min Liao, Zu-De Feng, and Zuo-Liang Chen. In situ tracing the process of human enamel demineralization by electrochemical impedance spectroscopy (EIS). *Journal of Dentistry*, 35:425–430, 2007.

[126] M-CDNJM. Huysmans, C. Longbottom, N.B. Pitts, P. Los, and P.G. Bruce. Impedance Spectroscopy of Teeth with and without Approximal Caries Lesionsan in vitro Study. *Journal of Dental Research*, 75(11):1871–1878, 1996.

[127] Zhang Xu, Koon GeeNeoh, and Anil Kishen. Monitoring acid-demineralization of human dentine by electrochemical impedance spectroscopy (EIS). *Journal of Dentistry*, 36:1005–1012, 2008.

[128] W.P. Rock and E.A.M. Kidd. The electronic detection of demineralisation in occlusal fissures. *British Dental Journal*, 164:243–247, 1988.

[129] K. Pieper, H. Visser, M. Hulsmann, and M. Wahner. Test of an electronic fissure caries detector. *Deutsche Zahnarztliche Zeitschrift*, 45:721–724, 1990.

[130] E.H. Verdonschot, E.M. Bronkhorst, R.C.W. Burgersdijk, K.G. König, M.J.M. Schaeken, and G.J. Truin. Performance of some diagnostic systems in examinations for small occlusal carious lesions. *Caries Research*, 26:59–64, 1992.

[131] D.N. Ricketts, E.A. Kidd, and R.F. Wilson. A re-evaluation of electrical resistance measurements for the diagnosis of occlusal caries. *British Dental Journal*, 178(205):11–17, 1995.

[132] N. Meredith and K. Gulabivala. Electrical impedance measurements of root canal length. *Endodontics & Dental Traumatology*, 13:126–131, 1997.

[133] Dejan Križaj, Janja Jan, and Vojko Valenčič. Modeling AC Current ConductionThrough a HumanTooth. *Bioelectromagnetics*, 25:185–195, 2004.

[134] Andréa Pereira Morais, Alexandre Visintainer Pino, and Marcio Nogueira Souza. Assessment of Tooth Structure using an Alternative Electrical Bioimpedance Spectroscopy Method. *Brazilian Dental Journal*, 25(2):146–152, 2014.

[135] Min-Huey Chen, Wei-Liang Chen, Yen Sun, Peter Tramyeon Fwu, Ming-Gu Lin, and Chen-Yuan Dong. Three-dimensional tooth imaging using multiphoton and second harmonic generation microscopy. *Proceedings of SPIE*, 6425, 2007.

[136] Po-Yen Lin, Hong-Chou Lyu, Chin-Ying Stephen Hsu, Chia-Seng Chang, and Fu-Jen Kao. Imaging carious dental tissues with multiphoton fluorescence lifetime imaging microscopy. *Biomedical Optics Express*, 2(1):149–158, 2010.

[137] Mostafa Fawzy Eissa, Hassan Mohamed El-Shamy, and Hassan Saad Hanafy. Structural and Dielectrical Properties of Sterilized Human Teeth. *Physics International*, 3(1):22–27, 2012.

[138] Hod Dana, Tsai-Wen Chen, Amy Hu, Brenda C. Shields, Caiying Guo, Loren L. Looger, Douglas S. Kim, and Karel Svoboda. Thy1-gcamp6 transgenic mice for neuronal population imaging in vivo. *PLoS ONE*, 9(9):108697, 2014.

[139] Adrian Wertz, Stuart Trenholm, Keisuke Yonehara, Daniel Hillier, Zoltan Raics, Marcus Leinweber, Gergely Szalay, Alexander Ghanem, Georg Keller,

Balázs Rózsa2, Karl-Klaus Conzelmann, and Botond Roska. Single-cell–initiated monosynaptic tracing reveals layer-specific cortical network modules. *Science*, 349(6243):70–74, 2015.

[140] Norbert Hájos, Tommas J. Ellender, Rita Zemankovics, Edward O. Mann, Richard Exley, Stephanie J. Cragg, Tamás F. Freund, and Ole Paulsen. Maintaining network activity in submerged hippocampal slices: importance of oxygen supply. *The European Journal of Neuroscience*, 29(2):319–327, 2009.

[141] Neuronexus. Data sheet of the microelectrode array for in vitro electrophysiology, page 93, last accessed: March 2021. https://neuronexus.com/wp-content/uploads/2020/09/2020-Probe-Catalog.pdf.

[142] R. Quian Quiroga, Z. Nadasdy, and Y. Ben-Shaul. Unsupervised Spike Detection and Sorting with Wavelets and Superparamagnetic Clustering. *Neural Computation*, 16(8):1661–1687, 2004.

[143] Michael S Lewicki. A review of methods for spike sorting: the detection and classification of neural action potentials. *Network: Computation in Neural Systems*, 9(4):R53–R78, 1998. PMID: 10221571.

[144] Kaylene C. Stocking, Alberto L. Vazquez, and Takashi D.Y. Kozai. Intracortical neural stimulation with untethered, ultrasmall carbon fiber electrodes mediated by the photoelectric effect. *IEEE Transactions on Biomedical Engineering*, 2019.

[145] Yi Qiang, Pietro Artoni, Kyung Jin Seo, Stanislav Culaclii, Victoria Hogan, Xuanyi Zhao, Yiding Zhong, Xun Han, Po-Min Wang, Yi-Kai Lo, Yueming Li, Henil A. Patel, Yifu Huang, Abhijeet Sambangi, Jung Soo V. Chu, Wentai Liu, Michela Fagiolini, and Hui Fang. Transparent arrays of bilayer-nanomesh microelectrodes for simultaneous electrophysiology and two-photon imaging in the brain. *Science Advances*, 4(9):eaat0626, 2018.

[146] Woodrow L. Shew, Timothy Bellay, and Dietmar Plenz. Simultaneous multi-electrode array recording and two-photon calcium imaging of neural activity. *Journal of Neuroscience Methods*, 192:75–82, 2010.

[147] Michael Z Lin; Mark J Schnitzer. Genetically encoded indicators of neuronal activity. *Nature Neuroscience*, 19:1142–1153, 2016.

[148] Rishikesh U. Kulkarni; Evan W. Miller. Voltage imaging: Pitfalls and potential. *Biochemistry*, 56(39):5171–5177, 2017.

[149] Vincent Villette; Mariya Chavarha; Ivan K. Dimov; Jonathan Bradley; Lagnajeet Pradhan; Benjamin Mathieu; Stephen W. Evans; Simon Chamberland; Dongqing Shi; Renzhi Yang; Benjamin B. Kim; Annick Ayon; Abdelali Jalil; Francois St-Pierre; Mark J. Schnitzer; Guoqiang Bi; Katalin Toth; Jun Ding; Stephane Dieudonne; Michael Z. Lin. Ultrafast two-photon imaging of a high-gain voltageindicator in awake behaving mice. *Cell*, 179(7):1590–1608, 2019.

[150] Aziza Eldarrat, Alec High, and Girish Kale. In vitro analysis of 'smear layer' on human dentine using ac-impedance spectroscopy. *Journal of Dentistry*, 32:547–554, 2004.

[151] T. MarjanovićI and I. Lacković. Dielectric Properties of Dentin between 100 Hz and 1 MHz Compared to Electrically Similar Body Tissues. In *XIII Mediterranean Conference on Medical and Biological Engineering and Computing*, pages 682–685, 2013.